Mutations differentially affecting the coronavirus Mac1 ADP-ribose binding and hydrolysis activities indicate that it promotes multiple stages of the viral replication cycle

Joseph J. O'Connor[1], Anuradha Roy[2], Reem Khattabi[1], Catherine Kerr[1], Nancy Schwarting[1], Yousef M. Alhammad[1], Philip Gao[3], Xiaoming Zhang[4], Xufang Deng[4,5], and Anthony R. Fehr[1]

[1]*Department of Molecular Biosciences, University of Kansas, Lawrence, Kansas 66045, USA*
[2]*Infectious Disease Assay Development (IDAD) Core, University of Kansas, Lawrence, Kansas 66047, USA*
[3]*Molecular Structures Group, University of Kansas, Lawrence, Kansas 66045, USA*
[4]*Department of Physiological Sciences, College of Veterinary Medicine, Oklahoma State University, Stillwater OK 74078, USA*
[5]*Oklahoma Center for Respiratory and Infectious Diseases, Oklahoma State University, Stillwater, Oklahoma 74078, United States.*

Correspondence: arfehr@ku.edu

Running title: Mac1 promotes multiple stages of the CoV lifecycle

Keywords: coronavirus, SARS-CoV-2, macrodomain, Mac1, ADP-ribose, nonstructural protein 3

ABSTRACT

All coronaviruses (CoVs) encode a conserved macrodomain, termed Mac1, in non-structural protein 3 (nsp3) that binds and hydrolyzes ADP-ribose covalently attached to proteins. Mac1 is a key virulence factor that counters antiviral ADP-ribosyltransferase (PARP) activity. Previously, we found that MHV strain JHM (JHMV) with a mutation in the adenine binding site, JHMV-D1329A, was extremely attenuated in all tested cell types as opposed to JHMV-N1347A, which only has a replication defect in bone-marrow derived macrophages (BMDMs). Interestingly, an N1347A/D1329A double mutant was unrecoverable, indicating an essential role for Mac1 in JHMV infection. We hypothesized that these mutations may impact different stages of the MHV lifecycle. First, to clarify how these mutations affected the biochemical activities of Mac1, we generated Mac1 proteins encoding the same mutations. As expected, the D-A mutation was extremely defective in ADP-ribose binding but maintained enzyme activity. In contrast, we previously found that the N-A mutation had WT levels of ADP-ribose binding but low enzyme activity, confirming that these mutations differentially effect the biochemical functions of Mac1. Following infection, D1329A displayed a large defect in the accumulation of viral RNA compared to WT or N1347A in all cells tested. Alternatively, N1347A infection produced normal levels of viral RNA but produced reduced levels of viral protein in interferon competent bone-marrow derived macrophages (BMDMs). These results suggest that Mac1 ADP-ribose binding and enzymatic activities promote different stages of the viral lifecycle, demonstrating the critical importance of Mac1 for JHMV replication.

41 **IMPORTANCE**

42 Over the last three decades, coronaviruses have repeatedly demonstrated their potential to become
43 significant veterinary and public health threats. Zoonotic transmission of the myriad known
44 coronavirus strains will remain a concern, regardless of the advances in vaccines and treatment.
45 One difficulty in anticipating the next coronavirus outbreak is their diverse lineage and high
46 propensity for mutation and recombination. The coronavirus macrodomain, Mac1, is conserved
47 amongst all known coronaviruses and is also conserved in the *Togaviridae* and *Hepeviridae*
48 families. Mac1 is a key factor in viral replication and pathogenesis, but its role in the replication
49 cycle remains unclear. A deeper investigation of Mac1 function will identify conserved antiviral
50 mechanisms and aid in the development of Mac1 inhibitors that represent a novel strategy for
51 antiviral therapeutics.

52

53 **INTRODUCTION**

54 Coronaviruses (CoVs) are large, positive-sense ssRNA viruses with unusually large genomes
55 ranging from 28-33 kb. Subdivided into four genera (alpha, beta, gamma, and delta), coronaviruses
56 cause disease of clinical and veterinary significance in mammals and birds. Deadly infections in
57 piglets with porcine endemic diarrhea virus illustrate the significant economic burden
58 coronaviruses impose on the livestock industry (1); however, recent history demonstrates zoonotic
59 transmission of CoVs to be an even greater economic and public health threat. Between 10-30%
60 of circulating common cold viruses in humans are caused by CoVs like hCoV-229E and hCoV-
61 OC43, which have a likely origin in zoonotic transmission from livestock(2, 3). The emergence of
62 three highly pathogenic human CoVs within as many decades has placed the threat of novel
63 zoonotic CoVs near the forefront of pandemic concern (4, 5). Efforts to determine the functions of
64 highly conserved CoV proteins will help aid in developing novel therapies to help mitigate future
65 outbreaks of divergent CoVs.

66 The CoV genome is organized into two major segments encoding the non-structural and the
67 structural proteins. Structural proteins such as the spike and nucleocapsid protein are encoded in
68 transcriptionally "nested" ORFs at the 3' end of the genome. The non-structural proteins (nsps) are
69 encoded at the 5' end in two large co-terminal ORFs that comprise about two-thirds of the genome.
70 Nsps are translated as large polyproteins from either ORF1a or from ORF1ab which are then
71 proteolytically processed into each of the functional nsps. Translational regulation between these
72 two ORFs is achieved through ribosomal frameshifting bypassing a conserved stop codon. It is
73 thought this strategy is meant to maintain optimal stoichiometric ratios between proteins important
74 for blocking immunity or establishing viral infection and the proteins that constitute the RNA
75 replication machinery (6).

76 Nsp3 is the largest of the coronavirus nonstructural proteins with a mass of approximately 220
77 kDa. Nsp3 contains numerous domains with important characterized functions. These include
78 polyprotein cleavage and deubiquitinase (DUB) activity of PL^{pro}, ssRNA and nucleocapsid binding
79 of Ubl1, ADP-ribosylhydrolase activity of the conserved macrodomain, and formation of
80 replication organelles (ROs) (7–10). Most notably, nsp3-4 dimers form large hexamers that, on
81 one side of the ER double membrane, complex with the replicase holoenzyme and, on the other
82 side, comprise a pore through which newly synthesized viral RNA is shuttled into the cytoplasm(9,
83 11–13). These findings establish nsp3 as a platform for multiple key steps of the replication cycle,
84 including the establishment of the RO, initial RNA replication, viral protein processing, and
85 packaging. Interestingly, in SARS-CoV-2 infection, nsp3 has also been shown to be distributed at
86 low levels throughout the cytoplasm, suggesting it may play additional roles in infection (14).

87 Within nsp3 reside up to three macrodomains termed Mac1, Mac2, and Mac3. Macrodomains are
88 a class of conserved protein domains present in all forms of life. Their structure, characterized by
89 a mixed α-β-α sandwich fold, is highly conserved, however their sequences – and therefore their
90 functions – are diverse (15). Mac2 and Mac3, originally identified in SARS-CoV as part of the
91 SARS-CoV Unique Domain (SUD), are present only in a subset of CoVs, most notably the
92 *Sarbecoviruses*, and were demonstrated to bind nucleic acid (16). Mac1, on the other hand, is
93 highly conserved across coronaviruses and has been shown to be a key virulence factor. Belonging
94 to the MacroD-type class of macrodomains, the CoV Mac1 targets and hydrolyses ADP-ribose
95 moieties, reversing a post-translational modification known as ADP-ribosylation (17–19).

96 ADP-ribosylation, the process by which ADP-ribose is covalently attached to target proteins, is
97 facilitated by enzymes known as ADP-ribosyltransferases (ARTs), commonly referred to as
98 PARPs. With 17 members in mammals, the PARP family regulates a myriad of cellular processes

99 such as stress granule formation, cellular trafficking, DNA damage repair, gene expression, and
100 cell cycle progression (20). Additionally, the importance of PARPs in the innate antiviral response
101 is increasingly clear. Many of the mono-ADP-ribosylating (MARylating) PARPs are IFN-
102 stimulated genes (ISGs) that modulate the inflammatory response and restrict viral replication (21–
103 23). Importantly, ADP-ribose can be added to several different types of residues, including basic
104 and acidic residues, as well as serine and cysteine (24, 25). Importantly, most macrodomains can
105 only remove ADP-ribose from acidic residues but still bind to ADP-ribose attached at other
106 residues. Thus, both ADP-ribose binding and hydrolysis can separately impact biological
107 functions. In CoVs, Mac1 activity is required for IFN repression and efficient viral replication,
108 though the exact targets remain unclear (26–31). Mac1 catalytic activity relies on a highly
109 conserved asparagine (residue N1347 in mouse hepatitis virus (MHV) strain JHM (JHMV)) which
110 coordinates critical hydrogen bonds with the distal ribose (32, 33). Previous characterizations of
111 an alanine mutation at this site abolished the catalytic activity of Mac1 and sensitized the virus to
112 type-I IFN (IFN-I) signaling but did not impact its ability to bind ADP-ribose (29, 34). In JHMV,
113 a N1347A mutant virus replicated normally in IFN-deficient cells such as 17Cl-1 but was
114 attenuated in IFN-competent bone-marrow derived macrophages (BMDMs). Importantly the
115 replication defect was lost in IFNAR knockout cells, demonstrating that Mac1 catalytic activity
116 counters IFN-mediated antiviral responses (34). Soon after, we also generated an alanine mutation
117 at D1329 in JHMV, a residue predicted to coordinate stabilizing interactions with the adenine
118 critical for substrate binding. This mutant demonstrated a large replication defect in both IFN-
119 competent and IFN-deficient cells, suggesting differential roles for the binding and hydrolysis
120 activity of Mac1 (29). Mutation in both residues resulted in a non-replicating virus that was unable
121 to be launched *de novo.* Unsurprisingly, a full in-frame deletion of Mac1 from either JHMV or

122 MERS-CoV resulted in unrecoverable viruses. Interestingly, however, SARS-CoV-2 tolerated the
123 deletion, but was sensitive to IFN-γ pre-treatment, similar to the SARS-CoV-2 N1062A mutant
124 virus (31). This result indicates that JHMV and MERS-CoV have a strict requirement for Mac1
125 ADP-ribose binding while SARS-CoV-2 may have evolved to encode for a protein with redundant
126 function. We recently found that mutation of a conserved isoleucine in MERS-CoV and SARS-
127 CoV-2 conferred enhanced Mac1 binding affinity to ADP-ribose with no impact on catalytic
128 activity but resulted in an overall reduction in viral replication (35). This data together indicates
129 that Mac1 is a critical factor in CoV replication and fitness during infection but relies on finely
130 tuned biochemical properties to promote virus replication and pathogenesis.

131 In this study, we sought to define the stages of the viral replication cycle reliant on both known
132 biochemical functions of Mac1, binding and catalysis. As predicted, we found that purified SARS-
133 CoV-2 and MERS-CoV D-A mutant proteins demonstrated a stark decrease in substrate affinity
134 which contrasted with the previously published N-A mutant protein. However, it retained
135 substantial enzymatic activity as opposed to the N-A mutant. Thus, the D-A and N-A Mac1 mutants
136 provide suitable models to better understand the role of ADP-ribose bindings versus hydrolysis in
137 the viral lifecycle. In cell culture, the JHMV D1329A mutant virus showed a marked defect in
138 RNA production, while the N1347A mutant virus resembled WT virus in RNA replication kinetics
139 but was significantly reduced for protein accumulation in IFN-competent cells. These results
140 provide a more refined understanding of the multiple mechanisms that Mac1 utilizes to promote
141 CoV replication.

142 **RESULTS**

143 **Mutation of conserved aspartic acid and asparagine residue to alanine dramatically reduces**
144 **ADP-ribose binding but maintains ADP-ribosylhydrolase activity.** Two highly conserved
145 residues in JHMV Mac1, N1347 and D1329 **(Fig. 1A)** were previously demonstrated to impact
146 viral fitness and virulence, though to different degrees and in a cell-type specific manner (29). To
147 compare the biochemical properties of the D-A mutation with the previously characterized N-A
148 mutation (29, 35), we performed several previously established ADP-ribose binding and
149 hydrolysis assays using purified SARS-CoV-2 and MERS-CoV Mac1 WT and D-A proteins. We
150 and others have been unable to produce MHV Mac1 protein, so SARS-CoV-2 and MERS-CoV
151 proteins were used instead. ADP-ribose binding assays include a differential scanning fluorimetry
152 (DSF) assay that measures thermal stability, a proximity-based AlphaScreen assay, and isothermal
153 calorimetry (ITC) which measures the thermodynamic properties of binding. Thermal stability of
154 the WT-Mac1 protein was demonstrated to be approximately 6°C higher than that of the D-A
155 protein at the endpoint concentration of 1M ADP-ribose **(Fig. 1B)**. In the AlphaScreen assay, the
156 D-A protein had a multi-log reduction in alpha counts compared to the WT protein **(Fig. 1C)**.
157 Finally, isothermal titration calorimetry (ITC) data showed that the K_D of Mac1 D-A to ADP-ribose
158 was ~16-fold higher than the WT-ADP-ribose interaction **(Fig. 1D)**. We also saw similar results
159 for each of these assays using MERS-CoV Mac1 WT and D-A proteins **(Fig. S1)**. These data
160 together demonstrate a marked defect in the Mac1 D-A protein's ability to bind to ADP-ribose and
161 distinguishes the D-A mutant from the N-A mutant, which was previously shown to bind ADP-
162 ribose at near WT levels (35). In addition, we performed an *in vitro* ADP-ribosylhydrolase assay
163 by co-incubating purified SARS-CoV-2 Mac1-WT and D-A proteins with mono-ADP-ribosylated
164 (MARylated) PARP10 and measured the loss of MAR signal from PARP10 by Western blotting,

165 as previously described (27). We found that Mac1-D-A retained substantial enzyme activity which
166 contrasts with Mac1-N-A which we previously found to be largely devoid of catalytic activity **(Fig.**
167 **1E)** (35) These results are consistent with results from alphavirus macrodomain studies. These
168 biochemical studies provide a stark delineation between the D-A and N-A mutant proteins as being
169 deficient in either binding or hydrolysis, respectively.

170 **MHV D1329A/D1330A virus is attenuated in cell culture and *in vivo*.** Previous work with the
171 JHMV single-nucleotide D1329A mutant virus revealed a high propensity for reversion *in vivo*,
172 indicating a high fitness cost compared to other viable Mac1 mutants (29). To prevent this
173 reversion, the JHMV-D1329A mutant virus was regenerated to contain a two-nucleotide
174 substitution using a bacterial artificial chromosome (BAC) based reverse genetic system (36). We
175 produced this virus in cell culture and confirmed that it had no reverting mutations. Furthermore,
176 to confirm that the defect is not due to second-site mutations produced during cloning, we
177 reintroduced the WT Mac1 sequence into the JHMV-D1329A BAC which was termed the
178 "repaired" D1329A (*rep*D1329). In addition, we fully sequenced the MHV genome from terminal
179 passages of D1329A and found no additional mutations in the viral genome. At low (0.1) and high
180 (1.0) MOI, this new JHMV-D1329A mutant virus demonstrated the same multi-log replication
181 defect in DBTs when compared to *rep*D1329 and N1347A viruses as previously described **(Fig.**
182 **2A-B)** (29). Importantly, intranasal infection of C57BL/6 with JHMV-D1329A resulted in no
183 lethality or weight loss as compared to infection with *rep*D1329 which resulted in ~25% mouse
184 survival and an average of more than 10% weight loss. These results indicate that this two-base
185 pair mutant D1329A virus, unlike the single-base pair mutant, was unable to revert to WT *in vivo*
186 **(Fig. 2C-D)**. We also engineered the orthologous mutation into MHV-A59, D1330A. The A59-
187 D1330A virus had a mild replication defect in cell culture **(Fig. 2E-G)** but replicated poorly *in*

188 *vivo* compared to WT virus **(Fig. 2H**), indicating that Mac1 ADP-ribose binding is critical across
189 multiple strains of MHV.

190 **JHMV-D1329A produces small plaques and demonstrates reduced infectivity in mouse cells**
191 **compared to *rep*D1329 and N1347A viruses.** The first notable hallmark of the JHMV-D1329A
192 virus infection was a substantial reduction in overall plaque size in both DBT and L929 cells **(Fig.**
193 **3A-B)**. We quantitated the size of D1329A plaques as compared to *rep*D1329 and N1347A viruses
194 and found that the D1329A plaques were on average about half the size of the plaques produced
195 by *rep*D1329 and N1347A on both DBT and L929 cells **(Fig. 3C-D)**. JHMV plaques are formed
196 by cell-cell syncytia mediated by the S protein (37). Thus, this phenotype is likely due to a severe
197 reduction in the production of S protein or its ability to traffic to the cell surface. A severe lack of
198 S protein production could be due to the inability to initiate infection in some cells. To determine
199 if JHMV-D1329A has a defect in initiating a productive infection we performed a plaquing
200 efficiency assay using DBT, L929, and HeLa cells expressing the MHV receptor (Hela-MVR).
201 Equal plaque forming units (PFU) of *rep*D1329, D1329A, and N1347A were plated on each cell
202 type and the number of plaques were determined. D1329A produced ~5-10-fold fewer plaques on
203 both DBT and L929 cells as compared to *rep*D1329 and N1347A, indicating that D1329A has a
204 substantial defect in the ability to initiate a productive infection. Interestingly, this defect may be
205 species specific, as no defect was observed in Hela-MVR cells which are of human origin but
206 express the MHV receptor **(Fig. 3E)**.

207 **JHMV-D1329A has no defect in genomic RNA delivery into cells.** To determine if the inability
208 of D1329A virus to initiate infection stems from a reduction in the entry of viral RNA into the
209 cytoplasm of infected cells, we measured intracellular genomic RNA levels at 2 hpi via RT-qPCR.
210 Each of the three indicated cell lines were infected with JHMV-*rep*D1329 and D1329A for two

211 hours; after which, the cells were trypsinized and washed three times with PBS to remove non-
212 infective virions then resuspended in TRIzol™ Reagent (Invitrogen). RT-qPCR revealed no
213 significant reduction in D1329A gRNA levels when compared with *rep*D1329, suggesting that the
214 plaquing defect is not due to a defect in viral entry **(Fig. 4)**.

215 **JHMV-D1329A virus is defective in genomic and sub-genomic RNA accumulation compared**
216 **to *rep*D1329 and N1347A viruses.** Next, we assayed the accumulation of viral genomic and sub-
217 genomic RNAs in both high and low MOI infections of DBT and L929 cells. Using RT-qPCR,
218 viral genomic- RNA (gRNA) and sub-genomic RNA6 (sgRNA6) levels were quantified over a 20-
219 hour period **(Fig. 5A-B)**. We used sgRNA6 as a marker for sub-genomic RNAs as the primers for
220 sgRNA6 gave the most robust results in our qPCR assay. At high MOI, the N1347A virus closely
221 resembled the *rep*D1329 virus, as viral sgRNA6 and gRNA levels increased substantially between
222 4 and 12 hpi in DBTs, while D1329A infected cells failed to produce any new viral transcripts
223 before 12hpi. This difference was most notable in sgRNA6, as *rep*D1329 and N1347A transcripts
224 were increased by nearly 3-logs over the D1329A virus. The D1329A infected cells did show
225 increasing RNA production after 12hpi, indicating a delay in transcription initiation, though the
226 levels never reached that of *rep*D1329 or N1347A infected cells **(Fig. 5A)**. Similarly, infection of
227 L929s showed approximately 10 to 100-fold increases in gRNA and sgRNA6 levels in the
228 *rep*D1329 and N1347A infected cells compared to D1329A throughout the course of infection
229 **(Fig. 5B)**. Similar results were seen at low MOI **(Fig. S2)**. To determine whether the defect in
230 D1329A RNA accumulation was due to targeted degradation of viral transcripts, infected L929
231 cells were treated with the Remdesivir metabolite GS-441524 at 10 hpi to arrest RdRp-mediated
232 transcription (38), after which viral transcripts were quantified at four-hour intervals until 22hpi
233 **(Fig. 5C)**. GS-441524 was not added until 10 hpi as earlier addition may have limited the amount

234 of RNA produced during D1329A infection making it unfeasible to detect RNA degradation. Viral
235 RNA synthesis increased in GS-441524 treated cells for a few hours, after which they stabilized,
236 as compared to RNA levels in untreated cells, which continued to increase. In both the *rep*D1329
237 and D1329A infections treated with GS-441524, there was no evidence of RNA degradation as
238 RNA levels did not significantly decrease through the course of the infection, indicating that there
239 is no increased degradation of the D1329A transcripts compared to *rep*D1329.
240 As a separate method to analyze viral RNA production, we performed confocal immuno-
241 fluorescence microscopy with probes for dsRNA, the hallmark RNA replication intermediate **(Fig.**
242 **6A)**. DBT cells were infected with *rep*D1329, D1329A, and N1347A at an MOI of 0.5 and cells
243 were fixed and stained for nsp3 and dsRNA at 8 hpi. While mock infected cells were devoid dsRNA
244 signal, *rep*D1329 and N1347A infected cells demonstrated robust dsRNA staining that co-localized
245 with nsp3, indicating the dsRNA represented viral RNAs. In contrast, D1329A infected cells had
246 minimal dsRNA despite having significant nsp3 staining. Quantitation of these images confirmed
247 that the D1329A virus produced significantly reduced levels of dsRNA but only mildly reduced
248 levels of nsp3 **(Fig. 6B)**. In addition, we measured the proportion of dsRNA that overlapped with
249 nsp3 (labeld as M1) and conversely the proportion of nsp3 that overlapped with dsRNA (labeled
250 as M2) in each image using a Mander's coefficient. We found that wherever dsRNA staining was
251 present, it almost always overlapped with nsp3 staining from each virus **(Fig. 6C, M1-green)**.
252 However, there were a couple of cases in D1329A infected cells where nsp3 staining did not
253 contain any overlapping dsRNA staining, unlike *repD*1329 or N1347A **(Fig. 6C, M2-red)**. This
254 result indicates that D1329A infected cells produced nsp3 but were unable to efficiently produce
255 RNA. N1347A, conversely, appeared to produce similar levels of nsp3 and dsRNA staining
256 compared to *rep*D1329. To further determine if D1329A can efficiently translate non-structural

257 proteins, we stained for nsp3 at 6 hpi, the earliest time point that we could detect it. Imaging
258 demonstrated that D1329A produced nsp3 at these early time points at levels that were reduced
259 but not significantly different from *rep*D1329 and N1347A **(Fig. S3A-B)**. The reduction in nsp3 is
260 likely due to already reduced RNA production in these cells, as more genomic RNA would lead to
261 increased production of nsps for the *rep*D1329 or N1347A viruses. In combination, these results
262 suggest that Mac1 ADP-ribose binding is required for efficient viral transcription initiation in
263 murine cells, whereas hydrolysis activity is likely dispensable in the earliest stages of replication.
264 **N1347A infected primary bone-marrow derived macrophages (BMDMs) produce WT levels**
265 **of viral RNA but have reduced N protein accumulation compared to *rep*D1329 virus.** We
266 previously demonstrated that both N1347A and D1329A mutants have similar replication defects
267 in primary macrophages when infected at low MOI, which could be partially rescued by treatment
268 with PARP inhibitors (29). However, N1347A replication could also be rescued in IFNAR and
269 PARP12 knockout cells, while D1329A replication was not, indicating these viruses may impact
270 different parts of the viral lifecycle in these cells (31, 34). First, we tested whether these viruses
271 had replication defects at high MOI so we could evaluate the viral lifecycle within a single cycle
272 of replication. As expected, both viruses had replication defects in BMDMs when infected at an
273 MOI of 1.5 **(Fig.7A)**. Specifically, D1329A virus titers were reduced almost 14-fold from
274 *rep*D1329, while N1347A titers were reduced 5-fold. Next, we evaluated the accumulation of viral
275 gRNA and sgRNA6. D1329A infection resulted in a significant reduction in both gRNA and
276 sgRNA6 levels at 9 hpi, while gRNA and sgRNA6 levels following N1374A infection were similar
277 to those of *rep*D1329, as seen in both DBT and L929 cells **(Fig. 7B)**. Specifically, sgRNA and
278 gRNA levels were mildly reduced at 9 hpi but increased at 12 hpi following N1347A infection,
279 though these differences were not significant. However, when we evaluated the production of viral

280 structural proteins, N1347A infected cells produced reduced levels of nucleocapsid (N) and spike
281 (S) proteins at 9 and 12 hpi **(Fig. 7C)**. When quantitating viral protein levels from multiple
282 experiments, the amount of N protein was significantly reduced almost 4-fold at 9 hpi compared
283 to *rep*D1329 infection, while at 12 hpi N protein was reduced 1.5-fold **(Fig. 7D)**.

284 Additionally, we evaluated nsp3 and N protein abundance by confocal
285 immunofluorescence in BMDMs. BMDMs were infected at an MOI of 0.5 before fixation and
286 staining for nsp3 and N protein at 9 hpi **(Fig. 8A)**. Nsp3 puncta were again observed across all
287 three viruses. Quantification showed the D1329A infected cells had 7.5-fold less nsp3 staining
288 compared to *rep*D1329, while nsp3 levels were only reduced 1.6-fold in N1347A infected cells,
289 neither of which were significant **(Fig. 8B, middle)**. In fact, in several cells infected with D1329A,
290 the level of nsp3 was at or just below the mean of the *rep*D1329 infected cells, again demonstrating
291 that D1329A can produce sufficient levels of nsp3 early in infection. This is in contrast to N protein
292 staining, which was reduced nearly 100-fold in D1329A infected cells and almost 10-fold in
293 N1347A infected cells **(Fig. 8B, right)**. However, the level of N protein staining in N1347A
294 infected cells was highly variable within individual cells, with some cells producing normal levels
295 of N protein, while others were dramatically reduced. As N1347A is restricted by IFN-induced
296 PARPs (34), these results suggest that the levels of PARP induction between individual cells may
297 fluctuate, resulting in inconsistent reductions in N protein production compared to *rep*D1329. But
298 in general, N1347A infected cells produced less N protein, but not nsp3, than the *rep*D1329
299 infected cells. These observations suggest that initial nsp3 synthesis is not substantially impacted
300 by Mac1, but that subsequent viral RNA or late protein production relies on the binding and
301 hydrolysis activities, respectively, of Mac1 to proceed efficiently.

302 **DISCUSSION**

303 The current understanding of the conserved CoV macrodomain relies largely on its
304 characterization as an ADP-ribosylhydrolase. Previous work has highlighted the importance of
305 PARP activity and Mac1's de-ADP-ribosylating activity on viral fitness and pathogenesis in both
306 coronaviruses and alphaviruses (39). We have previously generated alanine mutations in several
307 conserved residues of the Mac1 binding pocket. We found that mutation in a conserved asparagine
308 residue important for hydrolysis activity, N1347A in JHMV, attenuated the virus in primary
309 macrophages and sensitized it to PARP activity. We also found that mutating another conserved
310 residue predicted to coordinate binding affinity, D1329, conferred a greater replication defect for
311 this virus. Finally, we have been unable to recover JHMV that incorporates both mutations or a
312 full Mac1 deletion. These findings led us to hypothesize that Mac1 is critical for JHMV infection
313 and serves multiple roles in the viral replication cycle.

314 In this study, we sought to determine the stages of the viral life cycle most reliant on the
315 binding and hydrolysis activity of Mac1 in an effort to better understand the roles Mac1 plays in
316 infection. To characterize the biochemical impacts of the conserved aspartic acid and asparagine
317 residues in the ADP-ribose binding pocket, we utilized purified SARS-CoV-2 and MERS-CoV
318 Mac1 proteins with each mutated to alanine and then performed *in vitro* ADP-ribose binding and
319 hydrolysis assays. These data demonstrated a stark delineation between these mutant Mac1
320 proteins and their ADP-ribose binding and hydrolysis activities. Previous work from our group
321 established the N-A mutant Mac1 suffered little to no loss in substrate binding affinity but had
322 greatly reduced hydrolysis (35) while here we found that the D-A mutant Mac1 had a multi-log
323 reduction in binding affinity, but only a slight reduction in hydrolysis. Importantly, similar results
324 were demonstrated by other groups with SARS-CoV-2 mutant proteins and with recombinant

325 alphavirus macrodomain proteins as well (33, 40). Next, we sought to compare the impact of both
326 mutations on viral replication in the early viral life cycle. To achieve this, we utilized the previously
327 generated JHMV-N1347A virus and re-generated a new clone of the previously studied D1329A
328 virus. This new clone was generated via a two base-pair substitution in the D1329 codon rather
329 than one to reduce the likelihood of reversion. As expected, this virus demonstrated severe
330 attenuation in cell culture and *in vivo*. Through the detection of dsRNA by confocal microscopy
331 and specific determination of viral genomic and sub-genomic RNA levels by qPCR, we found that
332 the D1329A virus does not efficiently initiate viral RNA production following infection of any
333 murine cell line that is susceptible to JHMV **(Figs. 5-6)**. Furthermore, the D1329A virus produced
334 similar amounts of nsp3 in BMDMs as *rep*D1329 virus, and puncta of nsp3 staining in D1329A
335 infected cells often lacked any notable dsRNA staining. In contrast, the N1347A virus replicated
336 viral RNA at levels equal to that of WT virus in all cell lines tested but had a notable defect in viral
337 protein production in primary BMDMs **(Fig. 7)**. These data indicate that the binding activity of
338 Mac1 is key for early RNA production, while the hydrolysis activity is important for accumulation
339 of viral proteins later on in the replication cycle. However, we cannot rule out the possibility that
340 other defects, such as in polyprotein processing or assembly, may also be present. In fact,
341 considering the level of N protein in N1347A infected BMDMs was almost back to WT levels at
342 12 hpi, it seems likely that there may be further defects in the assembly process for this virus.
343 Below we present several hypotheses for how each activity may promote replication.
344 *ADP-ribosylhydrolase activity.* We have demonstrated that PARP12 and PARP14 are both required
345 to restrict the replication of CoVs with catalytically inactive Mac1 (21, 31, 41). Others have found
346 that PARP14 is required for the production of ADP-ribose puncta following IFNγ or poly(I:C)
347 treatment (34). Within these puncta, both PARP14 and DTX3L, an E3 ubiquitin ligase, are likely

348 ADP-ribosylated, with DTX3L/PARP9 regulating the activity of PARP14 (42, 43). As an E3
349 ubiquitin ligase, it's possible that DTX3L ADP-ribosylation enhances its ability to target viral
350 proteins for degradation. However, there are many other potential targets of PARP14, such as p62,
351 an autophagy regulator, and RACK1, a ribosome binding protein, that could impact viral protein
352 production through autophagic degradation or repression of translation, respectively (44, 45).
353 Furthermore, PARP12 is localized to the Golgi and cell stress can trigger PARP12 movement from
354 the Golgi and a block in anterograde-membrane trafficking, which could impact viral assembly
355 (46). Further work is required to decipher which PARP12/14 target(s) restrict viral protein
356 production or assembly following infection with Mac1 catalytic-mutant CoVs.
357 *ADP-ribose binding activity.* We envision two separate but not mutually exclusive hypotheses for
358 how this Mac1 function promotes viral RNA production. Recent work has demonstrated that nsp3
359 plays a major role in forming a hexameric complex that constitutes a pore in the replication
360 organelle, through which viral RNA is thought to pass (9, 11). As part of the larger pore structure,
361 the N-terminal domains of nsp3 extend into the cytoplasm, where one or more subunits may
362 interact with a number of host and viral factors. Previous work has established the association of
363 nsp3 with the nucleocapsid protein as a critical factor in establishing CoV infection (8, 47, 48).
364 Current models postulate that, since CoV gRNA serves as both the initial mRNA for nsp translation
365 and the template for RNA replication, N protein may shuttle gRNA into the replication organelle
366 via the nsp3 pore (8). Mutational analysis from several groups have demonstrated this relies largely
367 on the interaction of the N-terminal Ubl1 of nsp3 with multiple phosphorylated residues in the
368 serine and arginine-rich regions N1b and N2a of N protein (47–49). Other characterizations of the
369 CoV nucleocapsid have revealed that it is also ADP-ribosylated (50). From the current data, it
370 appears that the N protein is ADP-ribosylated only during infection, and the modification is

371 retained in the virion. Moreover, the modification was shown to be unaffected by catalytically
372 active Mac1. Thus, in our first hypothetical model, Mac1 would interact with an ADP-ribosylated
373 N protein, to promote the translocation of either the viral genome or N protein through the pore
374 **(Fig. 9A)**. Since N protein phosphorylation is reliant on host kinases (51) and ADP-ribosylation
375 may compete with phosphorylation on some residues, perhaps Mac1 binding to ADP-ribosylated
376 N evolved as an alternative measure to maintain the interaction between N protein and nsp3.
377 Identification of the sites of N protein ADP-ribosylation and mutation analysis would help clarify
378 how ADP-ribosylation affects N protein's ability to interact with nsp3.

379 However, the hypothesis best supported by the current data is that the ADP-ribose binding
380 affinity of Mac1 serves to prevent a key antiviral host factor from disrupting the initiation of viral
381 transcription. Plaquing efficiency assays from this study showed that the D1329A mutant virus
382 more readily establishes productive infections in HeLa-MVR cells than in murine DBT or L929
383 cells, suggesting a host-dependent anti-viral response. Furthermore, treatment with PARP
384 inhibitors partially rescues D1329A virus replication, and treatment with the PARP substrate NAD^+
385 further reduces the replication of the D1329A virus (29). These results in combination suggests
386 there is a murine-specific host factor that restricts virus replication in an ADP-ribosylation
387 dependent manner. Binding of Mac1 to an unknown ADP-ribosylated host factor or factors may
388 prevent it from traversing the nsp3 pore to access the replication transcription complex (RTC) and
389 repress viral RNA production **(Fig. 9B)**. Structural analysis of the pore complex predicts a central
390 channel of around 17 Å (52) that may be large enough for small proteins to access the RTC.
391 Previous studies of related alphavirus macrodomain mutant viruses found that macrodomain/ADP-
392 ribose binding is also required for initiating efficient viral RNA synthesis, indicating that there
393 may be a conserved host mechanism that represses the initial transcription of multiple viruses (40,

394 53). Thus, future research into these mechanisms could identify novel methods for developing anti-

395 viral therapeutics targeting multiple classes of RNA viruses.

396 **METHODS**

397 **Cell Culture.** Delayed Brain Tumor (DBT), L929, 17CL-1, and HeLa cells expressing the MHV
398 receptor CEACAM1 (HeLa-MVR) were cultured in Dulbecco's modified Eagle medium
399 (Corning) supplemented with 10% fetal bovine serum, 100 U/ml penicillin, 100 mg/ml
400 streptomycin, 10mM HEPES, 1mM sodium pyruvate, 0.1mM nonessential amino acids, and 2mM
401 L-glutamine. Bone marrow-derived macrophages (BMDMs) were sourced from WT C57BL/6
402 mice and differentiated to M0 via culturing for 7 days in Roswell Park Memorial Institute medium
403 (RPMI) supplemented with 10µg/ml Macrophage Colony Stimulating Factor (MCSF) (Genscript)
404 in addition to 10% fetal bovine serum 100 U/ml penicillin, 100 mg/ml streptomycin, 10mM
405 HEPES, 1mM sodium pyruvate, 0.1mM nonessential amino acids, and 2mM L-glutamine.
406 Differentiation into M2 macrophages was conducted was achieved by the further addition of
407 10µg/ml IL-4 (Peprotech Inc.) preceding infection by 24 hours.

408 **Mice.** Pathogen-free C57BL/6 mice originally sourced from Jackson Laboratories were bred and
409 maintained in the animal care facility at the University of Kansas as approved by the University of
410 Kansas Institutional Animal Care and Use Committee (IACUC) following guidelines set forth in
411 the *Guidelines for the Care and Use of Laboratory Animals.*

412 **Generation of Recombinant JHMV and A59 Constructs.** Recombinant pBAC-JHMV D1329A
413 constructs were generated using Red recombination. Double-base pair mutations in the nsp3 Mac1
414 were engineered using the Kan^r-I-SceI marker cassette as previously described, using primers
415 listed in **Table 1**. Purified BAC DNA from Cml^r Kan^s colonies were analyzed by restriction
416 enzyme digest, PCR and full plasmid sequencing for validation of correct clones. Primers used for
417 validation of correct clones are also listed in **Table 1**. The recombinant MHV-A59 D1330A mutant
418 was generated as described previously (54, 55). The D1330A mutation was introduced using site-

419 direct mutagenesis (Q5 Site-Directed Mutagenesis Kit, E0554S, NEB England Biolabs) and
420 sequencing-validated. The full-length viral cDNA was assembled using T4 DNA ligase (M0202L,
421 NEB England Biolabs). The full-length viral RNA was synthesized using an in vitro transcription
422 kit (mMESSAGE mMACHINE T7 Transcription Kit, AM1344, Thermo Fisher Scientific)

423 **Reconstitution of recombinant pBAC-JHMV-derived virus.** Approximately 1×10^6 BHK-MVR
424 cells were transfected with approximately 0.5-1 μg of pBAC-JHMV DNA and 1 μg of pcDNA-
425 MHV-N plasmid or 1 μg of full-length A549 RNA using Polyjet (SignaGen) as a transfection
426 reagent. Virus stocks were created by infecting ~1.5×10^7 17Cl-1 cells at an MOI of 0.1 plaque-
427 forming units (PFU)/cell and collecting both the cells and supernatant at 16-20 hpi. The cells were
428 freeze-thawed, and debris was removed prior to collecting virus stocks. Virus stocks were
429 quantified by plaque assay on Hela-MVR cells and sequenced by collecting infected 17Cl-1 or
430 L929 cells using TRIzol™ Reagent (Invitrogen). The RNA from JHMV virions was likewise
431 isolated from infected cells and submitted for full genome sequencing (SeqCenter).

432 **Virus Replication Assay.** Cells were infected at the specified multiplicities of infection (MOIs)
433 via a 1-hour adsorption phase with a minimum working volume of DMEM containing virus
434 particles incubated at 37°C and periodically rocked to ensure complete coverage. Infected cells
435 and supernatants were collected by freeze-thaw at -80°C. Viral titers were determined via plaque
436 assay using HeLa-MVR cells.

437 **Plaque Size Measurements.** JHMV was serially diluted and plated onto monolayers of indicated
438 cell types in 24-well tissue culture plates. At 18hpi (DBT) or 20hpi (L929), cells were imaged
439 using an Accu-Scope® EXI-310 with an attached Excelis™ HDS Digital Imaging System. Plaque
440 diameters were measured using CaptaVision software calibrated with a stage micrometer.

441 **Plaque Reduction Assay.** Stocks of JHMV *rep*D1329, D1329A, and N1347A were serially diluted
442 and plated in triplicate on cell monolayers of HeLa, DBT, or L929 cells in 24-well tissue culture
443 plates. Plaque formation was assayed at 20hpi.
444 **Viral Entry Assay.** In a 24-well plate, DBT, L929, and HeLa cells were seeded at 2.25e5 cells/well
445 and infected with a 100µl volume of MHV-JHM at an MOI of 1 using a 1-hour adsorption phase
446 with regular shaking at 4°C. After the adsorption phase, cells were rinsed twice with PBS before
447 fresh media was added to each well and plates were subsequently returned to the incubator at 37°C.
448 At 2hpi, cells were removed from the incubator, rinsed with PBS, trypsinized, and the resulting
449 cell suspension was transferred to 1.5ml microcentrifuge tubes. Tubes were centrifuged at 7,500
450 rpm for 5 minutes and the resulting cell pellets were resuspended in fresh PBS. Cells were rinsed
451 in this fashion three times before a final resuspension in TRIzol™ Reagent (Invitrogen) frozen at
452 -80°C. RNA extraction was carried out following the manufacturer's recommended protocol.
453 **RT-qPCR Analysis.** Cell monolayers were treated with ice cold TRIzol™ Reagent (Invitrogen)
454 and RNA was extracted via the manufacturer's recommended protocol. Synthesis of cDNA was
455 conducted using random hexamers (Roche) with M-MuLV reverse transcriptase (NEB) via the
456 manufacturer's recommended instructions. Quantitation of cDNA transcripts was conducted using
457 the Quantstudio 3 Real-Time PCR system (ThermoFisher) using the SYBR™ Green Universal
458 Master Mix (ThermoFisher) with primers listed in **Table 2**.
459 **Mouse Infections.** For MHV mouse infections, 5-8 week-old male and female mice were
460 anesthetized with isoflurane and inoculated intranasally with 1×10^4 PFU recombinant JHMV or
461 intraperitoneally with 500 PFU of A59. To obtain tissue for A59 virus titers mice were euthanized
462 on different days post challenge, livers were removed and homogenized in phosphate buffered
463 saline (PBS), and titers were determined by plaque assay on either Hela-MVR (MHV) cells.

464 **Immunoblotting.** Total cell extracts were lysed in SDS-based lysis buffer containing Pierce™
465 Protease Inhibitor Cocktail (Thermo Scientific), PhosStop phosphatase inhibitor (Roche), 2% β-
466 mercaptoethanol, and 1 mM PMSF. Proteins were resolved on a 10% SDS-PAGE gel, transferred
467 to a polyvinylidene difluoride (PVDF) membrane, hybridized with a primary antibody, reacted
468 with an infrared (IR) dye-conjugated secondary anti- body, visualized using a Li-COR Odyssey
469 Imager (Li-COR), and analyzed using Image Studio software. Primary antibodies used for
470 immunoblotting included anti-MHV N monoclonal antibody (1:10,000), anti-MHV S monoclonal
471 antibody (1:5,000) (29), and anti-actin monoclonal antibody (1:10,000) (clone AC15; Abcam,
472 Inc.). Secondary IR antibodies were purchased from Li-COR.
473 **Immunofluorescence Staining.** Cells were seeded at approximately 1×10^5 cells/ well in 8 Well
474 Chamber, removable slides (ibidi) that were pre-coated with 50μg/ml collagen for 30 minutes.
475 Cells were infected at an MOI of 0.5. At each time point, cells were rinsed with Hank's Balanced
476 Salt Solution with 0.01% Sucrose (HBSS/Su) and fixed with the addition of 2% paraformaldehyde
477 in HBSS/Su. Permeabilization was conducted by rinsing 3x with HBSS/Su containing 0.1%
478 Saponin (HBSS/Su/Sap) before blocking with 3% normal goat serum in HBSS/Su/Sap. Primary
479 antibodies (mouse α-dsRNA clone rJ2, Millipore) (rabbit α-nsp3, in-house), each diluted 1:1,000
480 in HBSS/Su/Sap, were added at room temperature for 3 hours followed by rinsing 3× with
481 HBSS/Su/Sap. Goat-derived secondary antibodies (AlexaFluor 488/555) diluted 1:200 in
482 HBSS/Su/Sap were incubated 1 hour at room temperature protected from light followed by rinsing
483 twice with HBSS/Su/Sap, once with HBSS/Su, and once with HBSS. Nuclear staining was
484 achieved via the addition of 300nM DAPI in HBSS for 30 minutes followed by rinsing twice with
485 HBSS. Slides were finalized with the addition of Vectashield® hardening Mounting Media
486 (VectorLabs).

487 **Confocal Microscopy.** Images were collected with a Leica DM6-SPE upright laser-scanning
488 confocal microscope using a 63x oil-immersion objective lens with Type F oil. DAPI fluorescence
489 was achieved with a 405 excitiation and 430/80 emission. Goat anti-mouse ALEXA 488 was
490 imaged with 488 excitation 500/40 emission. Goat anti-rabbit ALEXA 555 was imaged with 561
491 excitation and 570/90 emission. Images were acquired using Leica LasX software.

492 **Quantification of Confocal Immunofluorescence.** Quantification of protein staining was
493 automated using a custom macro written in FIJI (ImageJ v.1.54f) (56). For each image, a median
494 3D filter was applied to multi-channel Z-stacks (x=1, y=1, z=1 for DBT; x=2, y=2, z=2 for
495 BMDM) after which maximum intensity Z-projections were generated, and the channels were
496 split. Regions of Interest (ROIs) were generated from these single-channel duplicates by automated
497 thresholding via the Moments, Triangle, and Renyientropy methods for the DAPI, dsRNA/N
498 protein, and nsp3 channels, respectively. Resulting binary masks were applied to the original Z-
499 projections and fluorescence intensity of staining was measured within regions of interest (ROIs)
500 on the relevant channel. The total area of each ROI was also recorded, and the Integrated Density
501 (IntDen) displayed is a product of the mean fluorescence intensity and the ROI area.

502 **Colocalization Analysis**

503 Manders' coefficients were obtained using the BIOP JACoP plugin for FIJI (ImageJ v.1.54f) (56,
504 57). Median filters (x=1, y=1) were applied to maximum projection z-stacks, after which Triangle
505 or RenyiEntropy auto thresholds were applied to the dsRNA and nsp3 channels, respectively.
506 Resulting ROIs were cropped to produce proportions of total dsRNA signal overlapped (M1) and
507 total nsp3 signal overlapped (M2).

508 **Protein Expression and Purification.** Recombinant proteins were produced as previously
509 described (35).

510 ***In vitro* de-MARylation Assay.** MARylated PARP10 was generated via the incubation of purified
511 GST-PARP10 with β-Nicotinamide Adenine Dinucleotide (β NAD^+) (Millipore-Sigma) in a
512 reaction buffer (50 mM HEPES, 150 mM NaCl, 0.2 mM DTT, and 0.02% NP-40). MARylated
513 PARP10 was aliquoted and stored at -80°C. Purified SARS-CoV-2 Mac1 WT and D-A were co-
514 incubated with MARylated PARP10 for indicated times at 37°C with a ratio of 1 μM Mac1 to 5
515 μM PARP10 in reaction buffer (50 mM HEPES, 150 mM NaCl, 0.2 mM DTT, and 0.02% NP-40).
516 The reaction was halted with the addition of 2X Laemmli sample buffer containing 10% β-
517 mercaptoethanol. Samples were then heated for five minutes at 95°C before loading into a Bolt™
518 4%-12% Bis-Tris Plus Gel in MES running buffer (ThermoFisher). Direct protein detection was
519 conducted via staining on a separate, identical gel using ReadyBlue® Protein gel stain (Sigma).
520 Transfer to polyvinylidene difluoride (PVDF) membrane was achieved via the iBlot™ 2 Dry
521 Blotting System (ThermoFisher). Immunoblotting of the MAR and GST signal was conducted
522 with anti-mono ADP-ribose binding reagent MABE1076 (Sigma) and an anti-GST monoclonal
523 antibody MA4-004 (ThermoFisher). Detection of primary antibodies was conducted using
524 secondary infrared anti-rabbit and anti-mouse antibodies (LI-COR Biosciences). Samples were
525 visualized using the Odyssey M® Imaging System (LI-COR Biosciences).
526 **Isothermal Titration Calorimetry.** All ITC titrations were performed on a MicroCal PEAQ-ITC
527 instrument (Malvern Pananalytical Inc., MA). All reactions were performed in 20 mM Tris pH 7.5,
528 150 mM NaCl using 100 μM of all macrodomain proteins at 25°C. Titration of 2 mM ADP-ribose
529 or ATP (MilliporeSigma) contained in the stirring syringe included a single 0.4 μL injection,
530 followed by 18 consecutive injections of 2 μL. Data analysis of thermograms was analyzed using
531 one set of binding sites model of the MicroCal ITC software to obtain all fitting model parameters
532 for the experiments. MERS-CoV and SARS-CoV-2 WT protein ITC data were previously

533 published (35). These experiments were performed alongside the mutant proteins, thus serving as
534 appropriate controls.

535 **Differential Scanning Fluorimetry.** Thermal shift assay with DSF involved use of LightCycler®
536 480 Instrument (Roche Diagnostics). In total, a 15 μL mixture containing 8X SYPRO Orange
537 (Invitrogen), and 10 μM macrodomain protein in buffer containing 20 mM Hepes, NaOH, pH 7.5
538 and various concentrations of ADP-ribose were mixed on ice in 384-well PCR plate (Roche).
539 Fluorescent signals were measured from 25 to 95 °C in 0.2 °C/30-s steps (excitation, 470-505 nm;
540 detection, 540-700 nm). Data evaluation and Tm determination involved use of the Roche
541 LightCycler® 480 Protein Melting Analysis software, and data fitting calculations involved the
542 use of single site binding curve analysis on GraphPad Prism.

543 **AlphaScreen Assay.** The AlphaScreen reactions were carried out in 384-well plates (Alphaplate,
544 PerkinElmer, Waltham, MA) in a total volume of 40 μL in buffer containing 25 mM HEPES (pH
545 7.4), 100 mM NaCl, 0.5 mM TCEP, 0.1% BSA, and 0.05% CHAPS. All reagents were prepared
546 as 4X stocks and 10 μL volume of each reagent was added to a final volume of 40 μL. After 1h
547 incubation at RT, streptavidin-coated donor beads (7.5 μg/mL) and nickel chelate acceptor beads
548 (7.5 μg/mL); (PerkinElmer AlphaScreen Histidine Detection Kit) were added under low light
549 conditions, and plates were shaken at 400 rpm for 60 min at RT protected from light. Plates were
550 kept covered and protected from light at all steps and read on BioTek plate reader using an
551 AlphaScreen 680 excitation/570 emission filter set. For data analysis, the percent inhibition was
552 normalized to positive (DMSO + labeled peptide) and negative (DMSO + macrodomain + peptide,
553 no ADPr) controls.

554 **Statistical Analysis.** A Student's *t* test was used to analyze differences in mean values between 2
555 groups, for multiple group comparisons, an ordinary one-way ANOVA was used. All results are

556 expressed as means ± standard errors of the means (SEM) unless stated as standard differentiation
557 (SD) or as geometric means ± 95% confidence internal. P values of ≤0.05 were considered
558 statistically significant (*, P≤0.05; **, P≤0.01; ***, P≤0.001; ****, P ≤0.0001; ns, not significant).
559 **Data and Materials Availability.** All data associated with this manuscript will be available
560 through the data repository FigShare at 10.6084/m9.figshare.c.7755170 at the time of publication.

ACKNOWLEDGEMENTS

We thank Ivan Ahel for providing protein expression plasmids, David Davido for critical reading, and the David Davido and Robin Orozco labs for helpful discussions. We thank our funding from the NIH, an NIH Graduate Training grant, the University of Kansas College of Liberal Arts and Sciences, and the Oklahoma Center for Advancement of Science & Technology.

Funding:
National Institutes of Health (NIH) grant R35GM138029 (ARF)
National Institutes of Health (NIH) grant P20GM113117 (ARF)
National Institutes of Health (NIH) grant K22AI134993 (ARF)
Oklahoma Center for Advancement of Science & Technology Health grant HR23-096 (XD)
NIH Graduate Training at the Biology-Chemistry Interface grant T32GM132061 (CMK)
University of Kansas College of Liberal Arts and Sciences Graduate Research Fellowship (CMK)

The funders had no role in study design, data collection and analysis, decision to publish, or preparation of the manuscript.

Author contributions:
Conceptualization: JJOC, ARF
Data curation: JJOC, AR, RK, CK, YMA, ARF
Formal analysis: JJOC, AR, RK, CK, YMA, ARF
Funding acquisition: ARF
Methodology: JJOC, AR, RK, CK, NS, ARF
Investigation: JJOC, AR, RK, CK, YMA, XZ, XD, ARF
Project administration: ARF
Resources: PG, XD, ARF
Visualization: JJOC, AR, RK, CK, YMA, ARF
Validation: JJOC, AR, ARF
Supervision: XD, ARF
Writing—original draft: JJOC, ARF
Writing—review & editing: JJOC, AR, RK, CK, NS, YMA, PG, XZ, XD, ARF

A.R.F. was named as an inventor on a patent filed by the University of Kansas for a live-attenuated SARS-CoV-2 vaccine

REFERENCES

1. Lin C-M, Saif LJ, Marthaler D, Wang Q. 2016. Evolution, antigenicity and pathogenicity of global porcine epidemic diarrhea virus strains. Virus Res 226:20–39.
2. Vijgen L, Keyaerts E, Lemey P, Maes P, Van Reeth K, Nauwynck H, Pensaert M, Van Ranst M. 2006. Evolutionary History of the Closely Related Group 2 Coronaviruses: Porcine Hemagglutinating Encephalomyelitis Virus, Bovine Coronavirus, and Human Coronavirus OC43. J Virol 80:7270–7274.
3. Corman VM, Eckerle I, Memish ZA, Liljander AM, Dijkman R, Jonsdottir H, Juma Ngeiywa KJZ, Kamau E, Younan M, Al Masri M, Assiri A, Gluecks I, Musa BE, Meyer B, Müller MA, Hilali M, Bornstein S, Wernery U, Thiel V, Jores J, Drexler JF, Drosten C. 2016. Link of a ubiquitous human coronavirus to dromedary camels. Proc Natl Acad Sci U S A 113:9864–9.
4. Paules CI, Marston HD, Fauci AS. 2020. Coronavirus Infections—More Than Just the Common Cold. JAMA 323:707.
5. Menachery VD, Yount BL, Debbink K, Agnihothram S, Gralinski LE, Plante JA, Graham RL, Scobey T, Ge X-Y, Donaldson EF, Randell SH, Lanzavecchia A, Marasco WA, Shi Z-L, Baric RS. 2015. A SARS-like cluster of circulating bat coronaviruses shows potential for human emergence. Nat Med 21:1508–13.
6. Hartenian E, Nandakumar D, Lari A, Ly M, Tucker JM, Glaunsinger BA. 2020. The molecular virology of coronaviruses. Journal of Biological Chemistry 295:12910–12934.
7. Lei J, Kusov Y, Hilgenfeld R. 2018. Nsp3 of coronaviruses: Structures and functions of a large multi-domain protein. Antiviral Res. Elsevier B.V. https://doi.org/10.1016/j.antiviral.2017.11.001.
8. Koetzner CA, Hurst-Hess KR, Kuo L, Masters PS. 2022. Analysis of a crucial interaction between the coronavirus nucleocapsid protein and the major membrane-bound subunit of the viral replicase-transcriptase complex. Virology 567:1–14.
9. Zimmermann L, Zhao X, Makroczyova J, Wachsmuth-Melm M, Prasad V, Hensel Z, Bartenschlager R, Chlanda P. SARS-CoV-2 nsp3 and nsp4 are minimal constituents of a pore spanning replication organelle https://doi.org/10.1038/s41467-023-43666-5.
10. Hagemeijer MC, Monastyrska I, Griffith J, van der Sluijs P, Voortman J, van Bergen en Henegouwen PM, Vonk AM, Rottier PJM, Reggiori F, De Haan CAM. 2014. Membrane rearrangements mediated by coronavirus nonstructural proteins 3 and 4. Virology 458–459:125–135.
11. Wolff G, Limpens RWAL, Zevenhoven-Dobbe JC, Laugks U, Zheng S, de Jong AWM, Koning RI, Agard DA, Grünewald K, Koster AJ, Snijder EJ, Bárcena M. 2020. A molecular pore spans the double membrane of the coronavirus replication organelle. Science (1979) 369:1395–1398.
12. Snijder EJ, Limpens RWAL, de Wilde AH, de Jong AWM, Zevenhoven-Dobbe JC, Maier HJ, Faas FFGA, Koster AJ, Bárcena M. 2020. A unifying structural and functional model of the coronavirus replication organelle: Tracking down RNA synthesis. PLoS Biol 18.
13. Chen A, Lupan AM, Quek RT, Stanciu SG, Asaftei M, Stanciu GA, Hardy KS, de Almeida Magalhães T, Silver PA, Mitchison TJ, Salic A. 2024. A coronaviral pore-replicase complex links RNA synthesis and export from double-membrane vesicles. Sci Adv 10:eadq9580.
14. Andronov L, Han M, Zhu Y, Balaji A, Roy AR, Barentine AES, Patel P, Garhyan J, Qi LS, Moerner WE. 2024. Nanoscale cellular organization of viral RNA and proteins in SARS-CoV-2 replication organelles. Nat Commun 15:1–17.
15. Rack JGM, Perina D, Ahel I. 2016. Macrodomains: Structure, Function, Evolution, and Catalytic Activities. Annu Rev Biochem 85:431–454.
16. Johnson MA, Chatterjee A, Neuman BW, Wüthrich K. 2010. SARS Coronavirus Unique Domain: Three-Domain Molecular Architecture in Solution and RNA Binding. J Mol Biol 400:724–742.

17. Fehr AR, Jankevicius G, Ahel I, Perlman S. 2018. Viral Macrodomains: Unique Mediators of Viral Replication and Pathogenesis. Trends Microbiol. Elsevier Ltd https://doi.org/10.1016/j.tim.2017.11.011.
18. Jankevicius G, Hassler M, Golia B, Rybin V, Zacharias M, Timinszky G, Ladurner AG. 2013. A family of macrodomain proteins reverses cellular mono-ADP-ribosylation. Nat Struct Mol Biol 20:508–14.
19. Egloff M-P, Malet H, Putics Á, Heinonen M, Dutartre H, Frangeul A, Gruez A, Campanacci V, Cambillau C, Ziebuhr J, Ahola T, Canard B. 2006. Structural and Functional Basis for ADP-Ribose and Poly(ADP-Ribose) Binding by Viral Macro Domains. J Virol 80:8493–8502.
20. Lüscher B, Ahel I, Altmeyer M, Ashworth A, Bai P, Chang P, Cohen M, Corda D, Dantzer F, Daugherty MD, Dawson TM, Dawson VL, Deindl S, Fehr AR, Feijs KLH, Filippov D V., Gagné JP, Grimaldi G, Guettler S, Hoch NC, Hottiger MO, Korn P, Kraus WL, Ladurner A, Lehtiö L, Leung AKL, Lord CJ, Mangerich A, Matic I, Matthews J, Moldovan GL, Moss J, Natoli G, Nielsen ML, Niepel M, Nolte F, Pascal J, Paschal BM, Pawłowski K, Poirier GG, Smith S, Timinszky G, Wang ZQ, Yélamos J, Yu X, Zaja R, Ziegler M. 2021. ADP-ribosyltransferases, an update on function and nomenclature. FEBS Journal https://doi.org/10.1111/febs.16142.
21. Fehr AR, Singh SA, Kerr CM, Mukai S, Higashi H, Aikawa M. 2020. The impact of PARPs and ADP-ribosylation on inflammation and host-pathogen interactions. Genes Dev 34:341–359.
22. Atasheva S, Frolova EI, Frolov I. 2014. Interferon-Stimulated Poly(ADP-Ribose) Polymerases Are Potent Inhibitors of Cellular Translation and Virus Replication. J Virol 88:2116–2130.
23. Li L, Zhao H, Liu P, Li C, Quanquin N, Ji X, Sun N, Du P, Qin CF, Lu N, Cheng G. 2018. PARP12 suppresses Zika virus infection through PARP-dependent degradation of NS1 and NS3 viral proteins. Sci Signal 11:535.
24. Hendriks IA, Larsen SC, Nielsen ML. 2019. An Advanced Strategy for Comprehensive Profiling of ADP-ribosylation Sites Using Mass Spectrometry-based Proteomics. Mol Cell Proteomics 18:1010–1026.
25. Buch-Larsen SC, Hendriks IA, Lodge JM, Rykær M, Furtwängler B, Shishkova E, Westphall MS, Coon JJ, Nielsen ML. 2020. Mapping Physiological ADP-Ribosylation Using Activated Ion Electron Transfer Dissociation. Cell Rep 32:108176.
26. Leung AKL, Griffin DE, Bosch J, Fehr AR. 2022. The Conserved Macrodomain Is a Potential Therapeutic Target for Coronaviruses and Alphaviruses. Pathogens 11(1):94.
27. Alhammad YMO, Kashipathy MM, Roy A, Gagné J-P, McDonald P, Gao P, Nonfoux L, Battaile KP, Johnson DK, Holmstrom ED, Poirier GG, Lovell S, Fehr AR. 2021. The SARS-CoV-2 Conserved Macrodomain Is a Mono-ADP-Ribosylhydrolase. J Virol 95(3):e01969-20.
28. Alhammad YMO, Fehr AR. 2020. The viral macrodomain counters host antiviral ADP-ribosylation. Viruses 12:1–12.
29. Voth LS, O'Connor JJ, Kerr CM, Doerger E, Schwarting N, Sperstad P, Johnson DK, Fehr AR. 2021. Unique Mutations in the Murine Hepatitis Virus Macrodomain Differentially Attenuate Virus Replication, Indicating Multiple Roles for the Macrodomain in Coronavirus Replication. J Virol 95(15):e0076621.
30. Heer CD, Sanderson DJ, Voth LS, Alhammad YMO, Schmidt MS, Trammell SAJ, Perlman S, Cohen MS, Fehr AR, Brenner C. 2020. Coronavirus infection and PARP expression dysregulate the NAD metabolome: An actionable component of innate immunity. Journal of Biological Chemistry 295:17986–17996.
31. Alhammad YM, Parthasarathy S, Ghimire R, Kerr CM, O'Connor JJ, Pfannenstiel JJ, Chanda D, Miller CA, Baumlin N, Salathe M, Unckless RL, Zuñiga S, Enjuanes L, More S, Channappanavar R, Fehr AR. 2023. SARS-CoV-2 Mac1 is required for IFN antagonism and efficient virus replication in cell culture and in mice. Proceedings of the National Academy of Sciences 120(35):e2302083120.

690 32. Correy GJ, Kneller DW, Phillips G, Pant S, Russi S, Cohen AE, Meigs G, Holton JM, Gahbauer S,
691 Thompson MC, Ashworth A, Coates L, Kovalevsky A, Meilleur F, Fraser JS. 2022. The mechanisms
692 of catalysis and ligand binding for the SARS-CoV-2 NSP3 macrodomain from neutron and x-ray
693 diffraction at room temperature Sci. Adv 8(21):eabo5083.
694 33. Rack JGM, Zorzini V, Zhu Z, Schuller M, Ahel D, Ahel I. 2020. Viral macrodomains: a structural and
695 evolutionary assessment of the pharmacological potential. Open Biol 10(11):200237.
696 34. Grunewald ME, Chen Y, Kuny C, Maejima T, Lease R, Ferraris D, Aikawa M, Sullivan CS, Perlman
697 S, Fehr AR. 2019. The coronavirus macrodomain is required to prevent PARP-mediated inhibition of
698 virus replication and enhancement of IFN expression. PLoS Pathog 15(5):e1007756.
699 35. Kerr CM, Pfannenstiel JJ, Alhammad YM, O'Connor JJ, Ghimire R, Shrestha R, Khattabi R,
700 Saenjamsai P, Parthasarathy S, McDonald PR, Gao P, Johnson DK, More S, Roy A, Channappanavar
701 R, Fehr AR. 2024. Mutation of a highly conserved isoleucine residue in loop 2 of several β-coronavirus
702 macrodomains indicates that enhanced ADP-ribose binding is detrimental for replication. J Virol
703 98(11):e0131324.
704 36. Fehr AR. 2020. Bacterial artificial chromosome-based lambda red recombination with the I-Scei
705 homing endonuclease for genetic alteration of MERS-CoV. Methods in Molecular Biology 2099:53–
706 68.
707 37. Yamada Y, Liu XB, Fang SG, Tay FPL, Liu DX. 2009. Acquisition of cell-cell fusion activity by amino
708 acid substitutions in spike protein determines the infectivity of a coronavirus in cultured cells. PLoS
709 One 4(7):e6130.
710 38. Yin W, Mao C, Luan X, Shen D-D, Shen Q, Su H, Wang X, Zhou F, Zhao W, Gao M, Chang S, Xie Y-
711 C, Tian G, Jiang H-W, Tao S-C, Shen J, Jiang Y, Jiang H, Xu Y, Zhang S, Zhang Y, Xu HE. Structural
712 basis for inhibition of the RNA-dependent RNA polymerase from SARS-CoV-2 by remdesivir Science
713 368(6498):1499-1504.
714 39. Ryan AP, Delgado-Rodriguez SE, Daugherty MD. 2025. Zinc-finger PARP proteins ADP-ribosylate
715 alphaviral proteins and are required for interferon-γ–mediated antiviral immunity. Sci Adv
716 11(5):eadm6812.
717 40. Abraham R, Hauer D, McPherson RL, Utt A, Kirby IT, Cohen MS, Merits A, Leung AKL, Griffin DE.
718 2018. ADP-ribosyl-binding and hydrolase activities of the alphavirus nsP3 macrodomain are critical
719 for initiation of virus replication. Proc Natl Acad Sci U S A 115:E10457–E10466.
720 41. Kerr CM, Parthasarathy S, Schwarting N, O'Connor JJ, Pfannenstiel JJ, Giri E, More S, Orozco RC,
721 Fehr AR. 2023. PARP12 is required to repress the replication of a Mac1 mutant coronavirus in a cell-
722 and tissue-specific manner. J Virol 97(9):e0088523.
723 42. Saleh H, Liloglou T, Rigden DJ, Parsons JL, Grundy GJ. 2024. KH-like Domains in PARP9/DTX3L
724 and PARP14 Coordinate Protein–Protein Interactions to Promote Cancer Cell Survival. J Mol Biol
725 436:168434.
726 43. Zhang Y, Mao D, Roswit WT, Jin X, Patel AC, Patel DA, Agapov E, Wang Z, Tidwell RM, Atkinson
727 JJ, Huang G, McCarthy R, Yu J, Yun NE, Paessler S, Lawson TG, Omattage NS, Brett TJ, Holtzman
728 MJ. 2015. PARP9-DTX3L ubiquitin ligase targets host histone H2BJ and viral 3C protease to enhance
729 interferon signaling and control viral infection. Nat Immunol 16:1215–1227.
730 44. Challa S, Nandu T, Kim HB, Gong X, Renshaw CW, Li W-C, Tan X, Aljardali MW, Camacho C V.,
731 Chen J, Kraus WL. 2025. RACK1 MARylation regulates translation and stress granules in ovarian
732 cancer cells. Journal of Cell Biology 224(2):e202401101.
733 45. Kubon D, Leslie Pedrioli DM, Hottiger MO. 2024. PARP14 mediated SQSTM1/p62 cysteine ADP-
734 ribosylation is counteracted by the SARS-CoV-2 macrodomain BioRxiv
735 https://doi.org/10.1101/2024.06.29.601315.

46. Catara G, Grimaldi G, Schembri L, Spano D, Turacchio G, Lo Monte M, Beccari AR, Valente C, Corda D. 2017. PARP1-produced poly-ADP-ribose causes the PARP12 translocation to stress granules and impairment of Golgi complex functions. Sci Rep 7(1):14035.
47. Hurst KR, Ye R, Goebel SJ, Jayaraman P, Masters PS. 2010. An Interaction between the Nucleocapsid Protein and a Component of the Replicase-Transcriptase Complex Is Crucial for the Infectivity of Coronavirus Genomic RNA. J Virol 84:10276–10288.
48. Cong Y, Ulasli M, Schepers H, Mauthe M, V'kovski P, Kriegenburg F, Thiel V, de Haan CAM, Reggiori F. 2020. Nucleocapsid Protein Recruitment to Replication-Transcription Complexes Plays a Crucial Role in Coronaviral Life Cycle. J Virol 94(4):e01925-19.
49. Keane SC, Giedroc DP. 2013. Solution Structure of Mouse Hepatitis Virus (MHV) nsp3a and Determinants of the Interaction with MHV Nucleocapsid (N) Protein. J Virol 87:3502–3515.
50. Grunewald ME, Fehr AR, Athmer J, Perlman S. 2018. The coronavirus nucleocapsid protein is ADP-ribosylated. Virology 517:62–68.
51. Wu C-H, Yeh S-H, Tsay Y-G, Shieh Y-H, Kao C-L, Chen Y-S, Wang S-H, Kuo T-J, Chen D-S, Chen P-J. 2009. Glycogen Synthase Kinase-3 Regulates the Phosphorylation of Severe Acute Respiratory Syndrome Coronavirus Nucleocapsid Protein and Viral Replication. Journal of Biological Chemistry 284:5229–5239.
52. Huang Y, Wang T, Zhong L, Zhang W, Zhang Y, Yu X, Yuan S, Ni T. 2024. Molecular architecture of coronavirus double-membrane vesicle pore complex. Nature 633:224–231.
53. Park E, Griffin DE. 2009. The nsP3 macro domain is important for Sindbis virus replication in neurons and neurovirulence in mice. Virology 388:305–314.
54. Deng X, StJohn SE, Osswald HL, O'Brien A, Banach BS, Sleeman K, Ghosh AK, Mesecar AD, Baker SC. 2014. Coronaviruses resistant to a 3C-like protease inhibitor are attenuated for replication and pathogenesis, revealing a low genetic barrier but high fitness cost of resistance. J Virol 88:11886–98.
55. Yount B, Denison MR, Weiss SR, Baric RS. 2002. Systematic assembly of a full-length infectious cDNA of mouse hepatitis virus strain A59. J Virol 76:11065–78.
56. Schindelin J, Arganda-Carreras I, Frise E, Kaynig V, Longair M, Pietzsch T, Preibisch S, Rueden C, Saalfeld S, Schmid B, Tinevez J-Y, White DJ, Hartenstein V, Eliceiri K, Tomancak P, Cardona A. 2012. Fiji: an open-source platform for biological-image analysis. Nat Methods 9:676–682.
57. BOLTE S, CORDELIÈRES FP. 2006. A guided tour into subcellular colocalization analysis in light microscopy. J Microsc 224:213–232.

769 **FIGURE LEGENDS**

770 **Fig. 1. Mutation of a highly conserved aspartic acid in the ADP-ribose binding pocket of**
771 **Mac1 dramatically reduces ADP-ribose binding but largely maintains its enzyme activity.**
772 **(A)** Highly conserved aspartic acid (red) and asparagine (green) residues highlighted in alignments
773 of coronavirus Mac1 and other related macrodomain proteins. **(B)** SARS-CoV-2 Mac1-WT and
774 D-A proteins were incubated with increasing quantities of ADP-ribose and then assayed for
775 thermal stability by differential scanning fluorimetry (DSF). **(C)** SARS-CoV-2 Mac1 WT and D-
776 A proteins were tested for their ability to interact with an ADP-ribosylated peptide using an
777 AlphaScreen assay. The results in B-C are representative of 2 independent experiments. **(D)**
778 Isothermal titration calorimetry (ITC) of purified SARS-CoV-2 WT and D-A proteins in the
779 presence of increasing concentrations of ADP-ribose. *SARS-CoV-2 WT protein was previously
780 published (27). The results are the combined averages of 4 independent experiments. **(E)** WT and
781 D-A proteins were incubated with MARylated GST-PARP10 CD for the indicated time and
782 MARylation levels were measured by Western blotting for mono-ADP-ribose. GST antibody was
783 used as a loading control. Results are from one experiment representative of 2 independent
784 experiments.

785 **Fig. 2. MHV-D1329A/D1330A virus is attenuated in cell culture and *in vivo.* (A-B)** DBT cells
786 were infected with JHMV-*rep*D1329, N1347A, and D1329A viruses at an MOI of 0.1 (A) and 1.0
787 (B). Progeny virus was collected at indicated times and was titered by plaque assay. The results
788 are from a single experiment representative of 2 independent experiments. **(C-D)** C57BL/6 mice
789 were infected with 10^4 PFU JHMV-*rep*D1329 and D1329A virus and monitored for survival (C)
790 and weight loss (D) over 12 days. n=9 mice, *rep*D1329; n=10 mice, D1329A. The results are the
791 combined data from two independent experiments. **(E-G)** DBT (E), L929 (F), and 17Cl-1 (G) cells

792 were infected with MHV-A59 WT and D1330A viruses and progeny virus was measured at 24 hpi.
793 The results are from a single experiment representative of 2 independent experiments. **(H)**
794 C57BL/6 mice were infected with 500 PFU A59-WT and D1330A viruses. Livers were collected
795 at 3 dpi in PBS and viral loads were measured by plaque assay. Graphs represent the geometric
796 mean with 95% confidence internal. n=7 mice, WT; n=9 mice, D1330A.

797 **Fig. 3. JHMV-D1329A virus produces small plaques and demonstrates reduced infectivity in**
798 **mouse cells compared to *rep*D1329 and N1347A viruses. (A-B)** DBT (A) and L929 (B) cells
799 were infected with JHMV-*rep*D1329 and D1329A at an MOI of 0.1 and were examined at 18
800 (DBT) or 20 (L929) hpi to determine relative plaque sizes between mutants. **(C)** Plaque sizes were
801 measured using CaptaVision software calibrated with a stage micrometer n=27, *rep*D1329; n=41,
802 D1329A; n=45, N1347A **(D)** Plaque sizes were measured using CaptaVision software calibrated
803 with a stage micrometer n=25, *rep*D1329; n=21, D1329A; n=33, N1347A The results represent
804 the combined results of 2 independent experiments. **(E)** Hela-MVR, DBT, and L929 cells were
805 infected with equal PFUs of each virus and the number of plaques were counted 20 hpi. The results
806 are from a single experiment representative of 3 independent experiments.

807 **Fig. 4. JHMV-D1329A virus has no defect in genomic RNA delivery into cells.** Indicated cell
808 lines were infected with JHMV *rep*D1329 and D1329A viruses for 1 hr, then trypsinized for 5
809 minutes and rinsed 3 times with PBS. The cells were then collected, RNA was harvested, and
810 genomic RNA levels were determined by qPCR using the ΔCt method and normalized to HPRT
811 mRNA. These data are from a single experiment representative of 2 independent experiments.

812 **Fig. 5. JHMV-D1329A virus is defective in the production of viral genomic RNA (gRNA) and**
813 **sub-genomic RNA6 (sgRNA6) compared to *rep*D1329 and N1347A viruses. (A-B)** DBT (A)
814 and L929 (B) cells were infected with indicated viruses at an MOI of 3.0. Cells were collected at

815 indicated times and gRNA (top) and sgRNA6 (bottom) were measured by qPCR using the ΔΔCT
816 method and normalized to HPRT. The data in A-B is from a single experiment representative of 2
817 independent experiments. **(C)** L929 cells were infected with either *rep*D1329 or D1329A viruses
818 at an MOI of 0.1. At 10 hpi cells were treated with Remdesivir metabolite GS-441524 or DMSO
819 control. Cells were collected at indicated time points and viral gRNA (left) or sgRNA6 (right)
820 levels were determined by qPCR using the ΔΔCt method and normalized to HPRT mRNA. The
821 results are from a single experiment representative of 2 independent experiments.

822 **Fig. 6. JHMV-D1329A virus has reduced dsRNA levels early in infection. (A)** DBTs were
823 infected with indicated virus at an MOI of 0.5, fixed at 8 hpi, stained for dsRNA and nsp3, and
824 analyzed by confocal microscopy. **(B)** Quantification of fluorescence signal displayed as a product
825 of mean pixel intensity and thresholded area (IntDen). Error bars indicate geometric mean with
826 95% CI, combined data from two separate experiments. **(C)** Mander's coefficients displaying the
827 proportional overlap between regions where dsRNA overlaps nsp3 staining (M1 – green), and
828 where nsp3 staining overlaps dsRNA (M2 – red). Error bars indicate mean with 95% CI, combined
829 data from two separate experiments.

830 **Fig. 7. N1347A infected BMDMs produce WT levels of viral RNA but have reduced N protein**
831 **accumulation compared to *rep*D1329 virus. (A)** M2 differentiated BMDMs were infected with
832 indicated viruses at an MOI of 1.5. Cells and supernatants were collected at 18 hpi and progeny
833 virus was measured by plaque assay. The results are from a single experiment representative of 2
834 independent experiments. **(B)** BMDMs were infected as in (A) and cells were collected at indicated
835 times points and gRNA (left) and sgRNA6 (right) were measured by qPCR using the ΔCt method
836 and normalized to HPRT mRNA. The data in B represent the combined results of 3 (sgRNA6) or
837 4 (gRNA) independent experiments. **(C)** BMDMs were infected as in (A) and cells were collected

838 in sample buffer at indicated times points and viral spike (S) and nucleocapsid (N) proteins were
839 analyzed by Western blotting. Actin was used as a loading control. The results are from a single
840 experiment representative of 2-4 independent experiments. **(D)** Quantitation of the western blot
841 signal in C normalized to actin using Image J. The data in (D) represent the combined results from
842 4 (*rep*D1239 & N1347A) or 3 (D1329A) independent experiments.

843 **Fig. 8. D1329A and N1347A infected BMDMs have near *rep*D1329 levels of nsp3 but have**
844 **reduced N protein abundance. (A)** BMDMs were infected with indicated virus at an MOI of 0.5
845 and fixed at 9 hpi, stained for nsp3 and N protein, and analyzed by confocal microscopy. **(B)**
846 Quantification of fluorescence signal displayed as a product of mean pixel intensity and
847 thresholded area (IntDen) for all three fluorescent channels. Combined data from two independent
848 experiments presented as geometric mean with 95% confidence intervals.

849 **Fig. 9. Potential roles for Mac1 in regulating early RNA transcription. (A)** The Ubl1 domain
850 of nsp3 interacts with phosphorylated residues on the RNA-bound nucleocapsid protein which is
851 a key factor in shuttling viral RNA through the nsp3 pore to the site of transcription. Mac1 binding
852 affinity may enhance this interaction between nsp3 and N protein, without which there is a delay
853 in transcription initiation. **(B)** Mac1 binding affinity may sequester or block ADP-ribosylated host
854 factors that target and inhibit viral transcription early in the replication cycle.

855 **SUPPLEMENTAL FIGURE LEGENDS**

856 **Fig S1. MERS-CoV Mac1 D-A protein has poor ADP-ribose binding affinity. (A)** Isothermal
857 titration caliorimetry of purified MERS-CoV WT D-A Mac1 protein incubated with ADP-ribose.
858 *MERS-CoV WT protein data was previously published (27). **(B)** MERS-CoV Mac1 WT and DA
859 proteins were tested for their ability to interact with an ADP-ribosylated peptide using an
860 AlphaScreen assay. The results in A-B are from a single experiment representative of at least 2
861 independent experiments.

862 **Fig S2. JHMV-D1329A virus is defective in the production of viral genomic RNA (gRNA)**
863 **and sub-genomic RNA6 (sgRNA6) compared to *rep*D1329 and N1347A viruses. (A-B)** L929
864 (A) and DBT (B) cells were infected with indicated viruses at an MOI of 0.1. Cells were collected
865 at indicated times and genomic and RNAs were measured by qPCR using the *ΔΔ*CT method
866 normalized to HPRT. Results are from one experiment representative of two independent
867 experiments.

868 **Fig. S3. JHMV-D1329A produces nsp3 in the early stages of infection. (A)** DBTs were infected
869 with indicated virus at an MOI of 0.5, fixed at 6 hpi, stained for nsp3, and analyzed by confocal
870 microscopy. **(B)** Quantification of fluorescence signal displayed as a product of mean pixel
871 intensity and total thresholded area (IntDen), representative of two independent experiments.

872 **TABLE 1. Linear recombination primers for engineering JHMV-D1329A**

		5' – 3'
Mac1 D1329A Mutant Generation		
MHV-JHM DA	F	TTCATGTATAACACCAAATGTTTGTTTTGTTAAAGGAGCGGTTATAAAGGTTTTGCGC**AGAGGATGACGACGATAAGTAGGG**
	R	CGATGACTTCAGCACCAACTCTGCGCAAAACCTTTATAACCGCTCCTTTAACAAAACAAA**GCCAGTGTTACAACCAATTAACC**

873 Nucleotides mutated are designated in red

874

875 **TABLE 2. qPCR and Sequencing primers**

		5' – 3'
qPCR Primers		
M. musculus HPRT	F	GCGTCGTGATTAGCGATGATG
	R	CTCGAGCAAGTCTTTCAGTCC
MHV gRNA	F	AGGGAGTTTGACCTTGTTCACC
	R	ATAATGCACCTGTCATCCTCG
MHV sgRNA	F	TATAAGAGTGATTGGCGTCC
MHV sgRNA6	R	GTGGGGCCACATTAACCACAAG
MHV sgRNA4	R	CTAATGCTAGGCGCAGAA
Sequencing Primers		
MHV Mac1	F	GGCTGTTGTGGATGGCAAGCA
	R	GCTTTGGTACCAGCAACGGAG
MERS Mac1	F	CCGTCTGCACCTCAGACTATC
	R	GCAGAGTTGTCTGTGCACAC

877

A

```
MHV-JHM|P0C6V1|/1315-1377      YGSCITPNVCFVKGDVIKVL----RRVGAEVIVNPANGRMAHGAGVAGAIAKAAGKAFINETADMVK
MHV-A59|P0C6V0|/1316-1378      YGSCITPNVCFVKGDVIKVV----RLVNAEVIVNPANGRMAHGAGVAGAIAEKAGSAFIKETSDMVK
hCoV-OC43|P0C6U7|/1269-1331    YGSCITPNVCFVKGDIIKVS----KLVKAEVVVNPANGHMVHGGGVAKAIAVAAGQQFVKETTNMVK
hCoV-229E|P0C6U2|/1273-1335    NAFLVHDNVAFYQGDVDTVV----NGVDFDFIVNAANENLAHGGGLAKALDVYTKGKLQRLSKEHIG
SARS-CoV|P0C6U8|/1010-1070     --LKLTDNVAIKCVDIVKEA----QSANPMVIVNAANIHLKHGGGVAGALNKATNGAMQKESDDYIK
SARS-CoV-2|P0DTC1|/1032-1092   --LKLTDNVYIKNADIVEEA----KKVKPTVVVNAANVYLKHGGGVAGALNKATNNAMQVESDDYIA
MERS-CoV|K9N638|/1115-1177     EHKVITECVTIVLGDAIQVA----KCYGESVLVNAANTHLKHGGGIAGAINAASKGAVQKESDEYIL
PEDV|P0C6Y4|/1291-1352         KPFYSYKNVDFYQGDFSDLV-----KLPCDFVVNAANEKLSHGGGIAKAIDVYTKGMLQKCSNDYIK
IBV|P0C6Y1|/1011-1074          PKFLEYK---TCVGDLTVVIAKALDEFKEFCIVNAANEHMTHGSGVAKAIADFCGLDFVEYCEDYVK
CHIKV|Q8JUX6|/1329-1381        TRAGCAPSYRVKRMDIA--------KNDEECVVNAANPRGLPGDGVCKAVYKKWPESFKNS------
HEV|P29324|/772-838            HQTARHRRLLFTYPDGSKVFAGSLFESTCTWLVNASNVDHRPGGGLCHAFYQRYPASFDAASFVMRD
MACROD1|Q9BQ69|/146-204        KDKQLNEKISLLRSDITKLE--------VDAIVNAANSSLLGGGGVDGCIHRAAGPLLTDECRTLQS
MACROD2|A1Z1Q3|/64-122         VKKSLTEKVSLYRGDITLLE--------VDAIVNAANASLLGGGGVDGCIHRAAGPCLLAECRNLNG
```

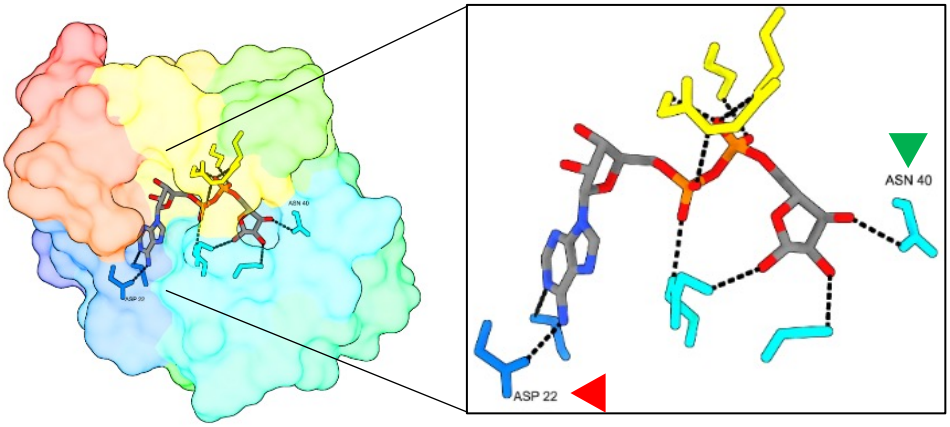

B

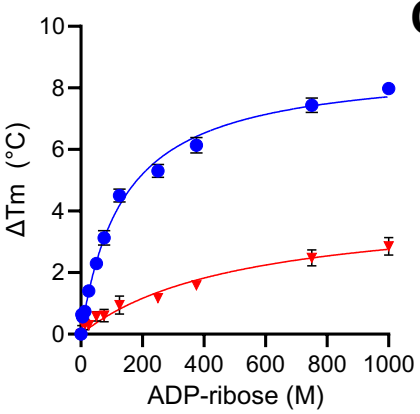

C

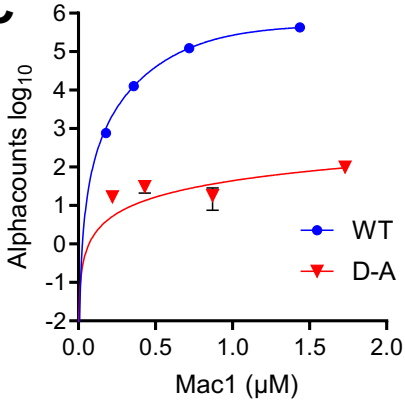

D

Macrodomain	Stoichiometry	Kd (μM)	ΔH (kcalmol^{-1})	ΔG (kcalmol^{-1})	-TΔS (kcalmol-1)
SARS-CoV-2 WT *	1	16.8 ± 0.42	-28 ± 0.07	-27.3 ± 0.07	0.5 ± 0.01
SARS-CoV-2 D-A	1	274.33 ± 6.35	-60.9 ± 3	-20.33 ± 0.1	40.53 ± 2.9

E

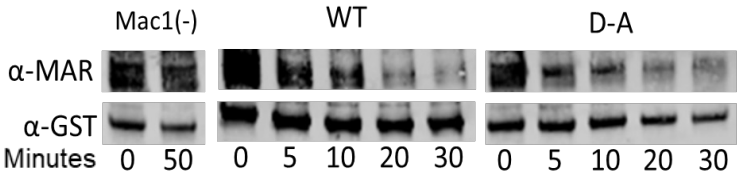

Fig. 1. Mutation of a highly conserved aspartic acid in the ADP-ribose binding pocket of Mac1 dramatically reduces ADP-ribose binding but largely maintains its enzyme activity. (A) Highly conserved aspartic acid (red) and asparagine (green) residues highlighted in alignments of coronavirus Mac1 and other related macrodomain proteins. **(B)** SARS-CoV-2 Mac1-WT and D-A proteins were incubated with increasing quantities of ADP-ribose and then assayed for thermal stability by differential scanning fluorimetry (DSF). **(C**) SARS-CoV-2 Mac1 WT and D-A proteins were tested for their ability to interact with an ADP-ribosylated peptide using an AlphaScreen assay. The results in B-C are representative of 2 independent experiments. (**D**) Isothermal titration calorimetry (ITC) of purified SARS-CoV-2 WT and D-A proteins in the presence of increasing concentrations of ADP-ribose. *SARS-CoV-2 WT protein was previously published (27). The results are the combined averages of 4 independent experiments. (**E)** WT and D-A proteins were incubated with MARylated GST-PARP10 CD for the indicated time and MARylation levels were measured by Western blotting for mono-ADP-ribose. GST antibody was used as a loading control. Results are from one experiment representative of 2 independent experiments.

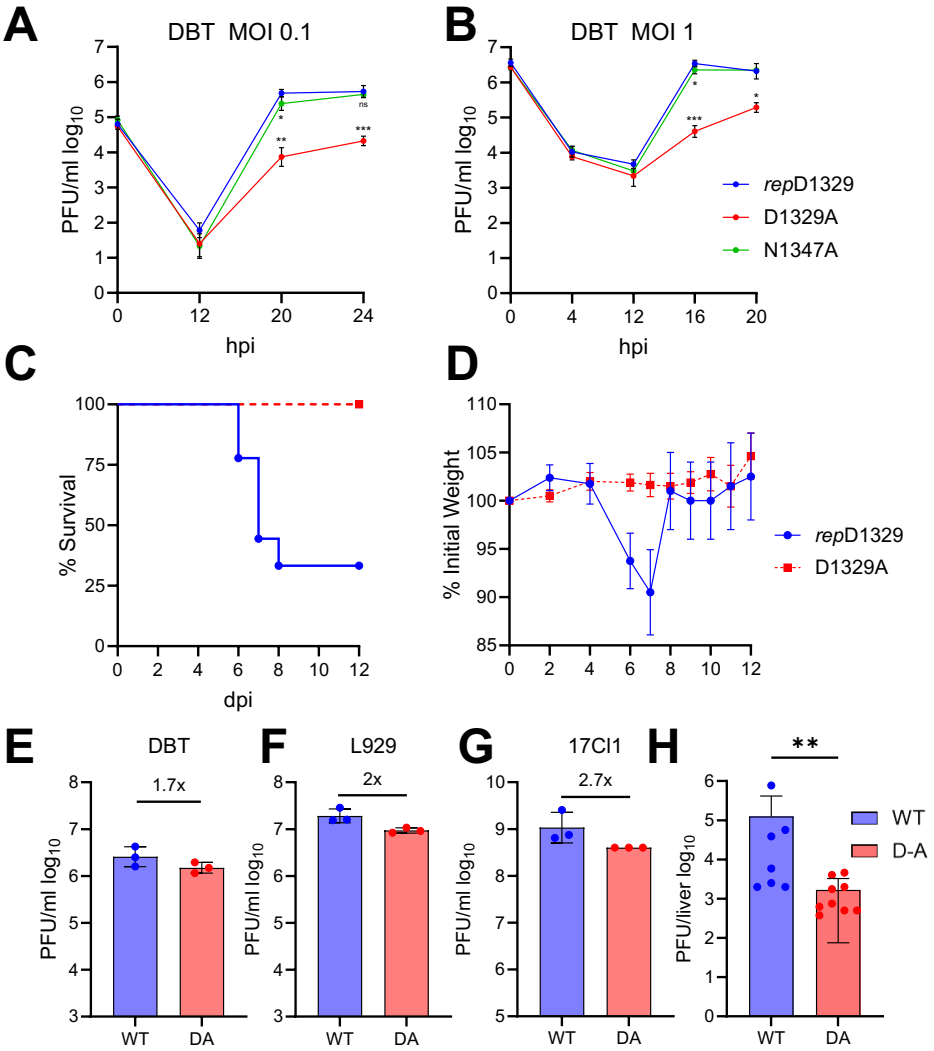

Fig. 2. MHV-D1329A/D1330A virus is attenuated in cell culture and *in vivo*. (A-B) DBT cells were infected with JHMV-*rep*D1329, N1347A, and D1329A viruses at an MOI of 0.1 (A) and 1.0 (B). Progeny virus was collected at indicated times and was titered by plaque assay. The results are from a single experiment representative of 2 independent experiments. **(C-D)** C57BL/6 mice were infected with 10^4 PFU JHMV-*rep*D1329 and D1329A virus and monitored for survival (C) and weight loss (D) over 12 days. n=9 mice, *rep*D1329; n=10 mice, D1329A. The results are the combined data from two independent experiments. **(E-G)** DBT (E), L929 (F), and 17Cl-1 (G) cells were infected with MHV-A59 WT and D1330A viruses and progeny virus was measured at 24 hpi. The results are from a single experiment representative of 2 independent experiments. **(H)** C57BL/6 mice were infected with 500 PFU A59-WT and D1330A viruses. Livers were collected at 3 dpi in PBS and viral loads were measured by plaque assay. Graphs represent the geometric mean with 95% confidence internal. n=7 mice, WT; n=9 mice, D1330A.

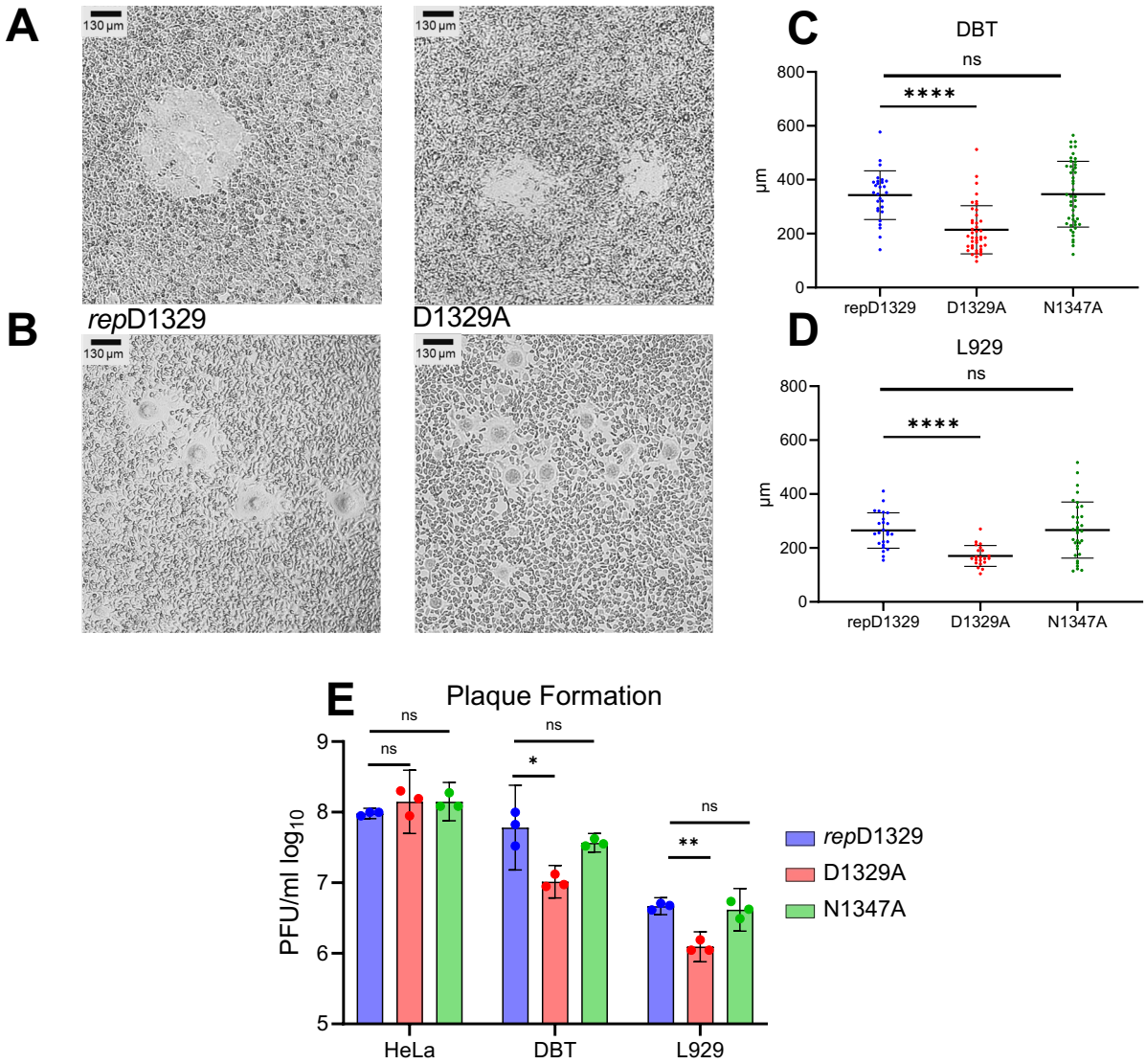

Fig. 3. JHMV-D1329A virus produces small plaques and demonstrates reduced infectivity in mouse cells compared to *rep*D1329 and N1347A viruses. (A-B) DBT (A) and L929 (B) cells were infected with JHMV-*rep*D1329 and D1329A at an MOI of 0.1 and were examined at 18 (DBT) or 20 (L929) hpi to determine relative plaque sizes between mutants. **(C)** Plaque sizes were measured using CaptaVision software calibrated with a stage micrometer n=27, *rep*D1329; n=41, D1329A; n=45, N1347A **(D)** Plaque sizes were measured using CaptaVision software calibrated with a stage micrometer n=25, *rep*D1329; n=21, D1329A; n=33, N1347A The results represent the combined results of 2 independent experiments. **(E)** Hela-MVR, DBT, and L929 cells were infected with equal PFUs of each virus and the number of plaques were counted 20 hpi. The results are from a single experiment representative of 3 independent experiments.

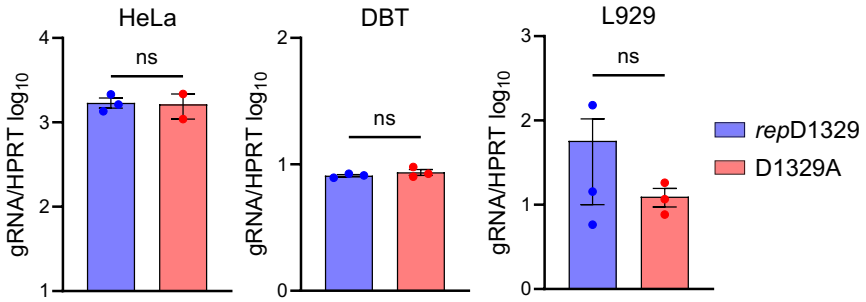

Fig. 4. JHMV-D1329A virus has no defect in genomic RNA delivery into cells. Indicated cell lines were infected with JHMV *rep*D1329 and D1329A viruses for 1 hr, then trypsinized for 5 minutes and rinsed 3 times with PBS. The cells were then collected, RNA was harvested, and genomic RNA levels were determined by qPCR using the *Δ*Ct method and normalized to HPRT mRNA. These data are from a single experiment representative of 2 independent experiments.

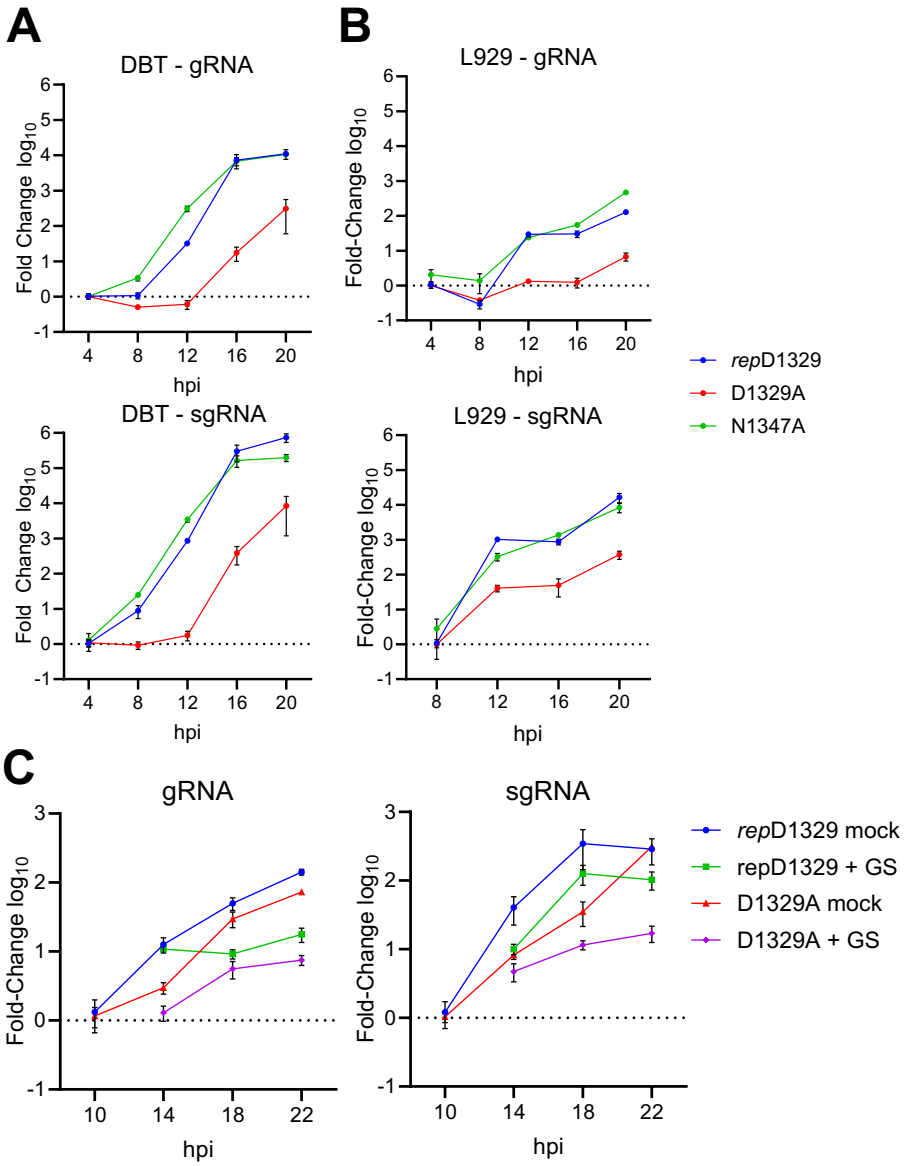

Fig. 5. JHMV-D1329A virus is defective in the production of viral genomic RNA (gRNA) and sub-genomic RNA6 (sgRNA6) compared to *rep*D1329 and N1347A viruses. (A-B) DBT (A) and L929 (B) cells were infected with indicated viruses at an MOI of 3.0. Cells were collected at indicated times and gRNA (top) and sgRNA6 (bottom) were measured by qPCR using the ΔΔCT method and normalized to HPRT. The data in A-B is from a single experiment representative of 2 independent experiments. **(C)** L929 cells were infected with either *rep*D1329 or D1329A viruses at an MOI of 0.1. At 10 hpi cells were treated with Remdesivir metabolite GS-441524 or DMSO control. Cells were collected at indicated time points and viral gRNA (left) or sgRNA6 (right) levels were determined by qPCR using the ΔΔCt method and normalized to HPRT mRNA. The results are from a single experiment representative of 2 independent experiments.

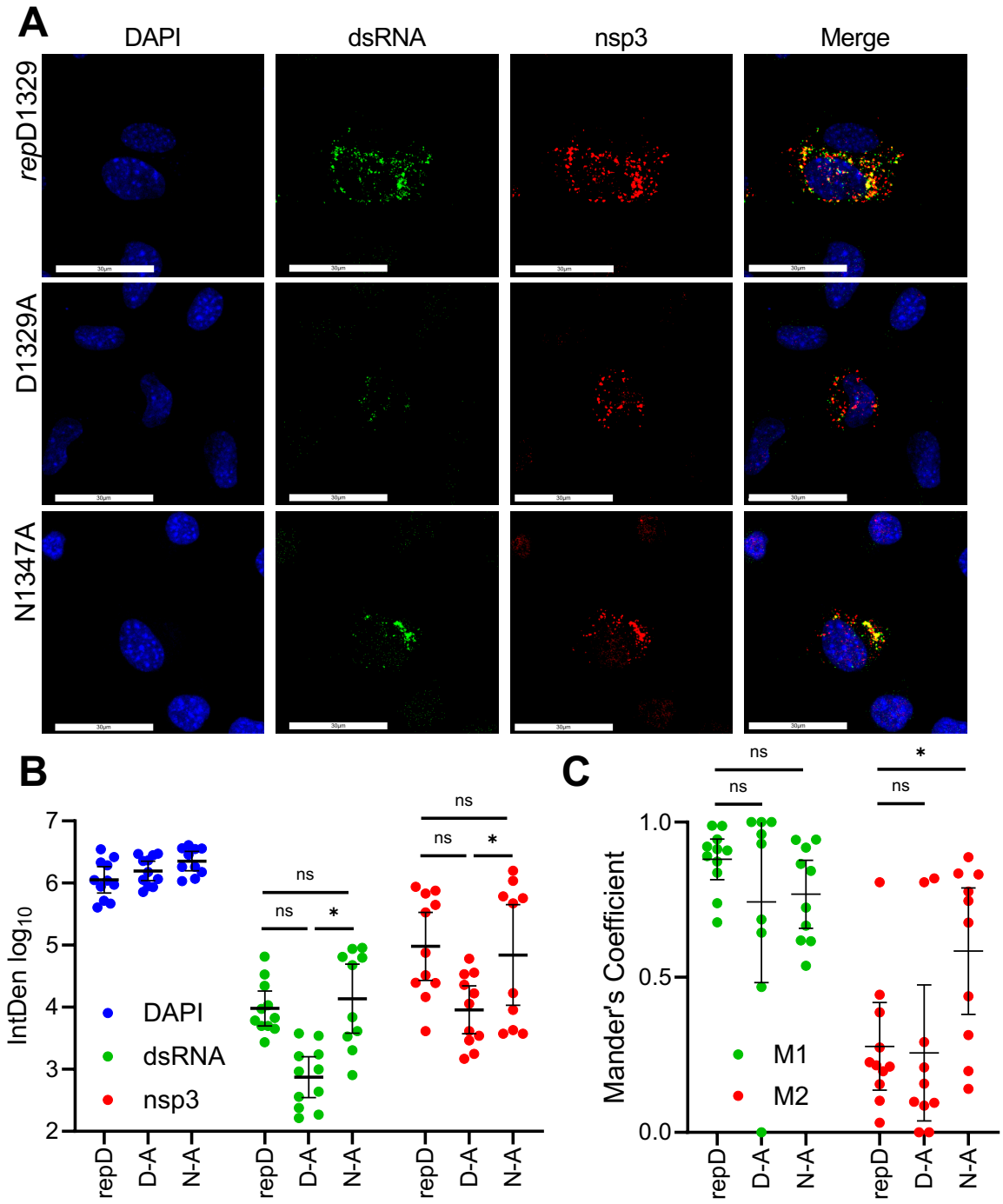

Fig. 6. JHMV-D1329A virus has reduced dsRNA levels early in infection. (A) DBTs were infected with indicated virus at an MOI of 0.5, fixed at 8 hpi, stained for dsRNA and nsp3, and analyzed by confocal microscopy. **(B)** Quantification of fluorescence signal displayed as a product of mean pixel intensity and thresholded area (IntDen). Error bars indicate geometric mean with 95% CI, combined data from two separate experiments. **(C)** Mander's coefficients displaying the proportional overlap between regions where dsRNA overlaps nsp3 staining (M1-green dots) and where nsp3 staining overlaps dsRNA (M2 – red dots). Error bars indicate mean with 95% CI, combined data from two separate experiments.

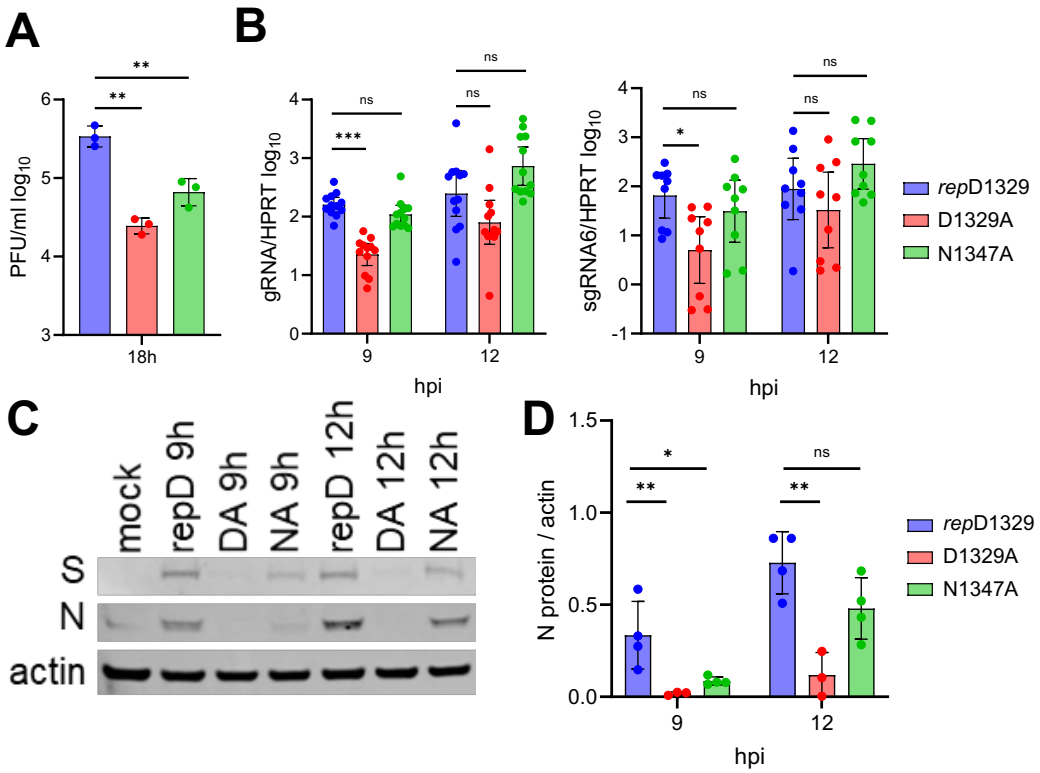

Fig. 7. N1347A infected BMDMs produce WT levels of viral RNA but have reduced N protein accumulation compared to *rep*D1329 virus. (A) M2 differentiated BMDMs were infected with indicated viruses at an MOI of 1.5. Cells and supernatants were collected at 18 hpi and progeny virus was measured by plaque assay. The results are from a single experiment representative of 2 independent experiments. **(B)** BMDMs were infected as in (A) and cells were collected at indicated times points and gRNA (left) and sgRNA6 (right) were measured by qPCR using the *Δ*Ct method and normalized to HPRT mRNA. The data in B represent the combined results of 3 (sgRNA6) or 4 (gRNA) independent experiments. **(C)** BMDMs were infected as in (A) and cells were collected in sample buffer at indicated times points and viral spike (S) and nucleocapsid (N) proteins were analyzed by Western blotting. Actin was used as a loading control. The results are from a single experiment representative of 2-4 independent experiments. **(D)** Quantitation of the western blot signal in C normalized to actin using Image J. The data in (D) represent the combined results from 4 (*rep*D1239 & N1347A) or 3 (D1329A) independent experiments.

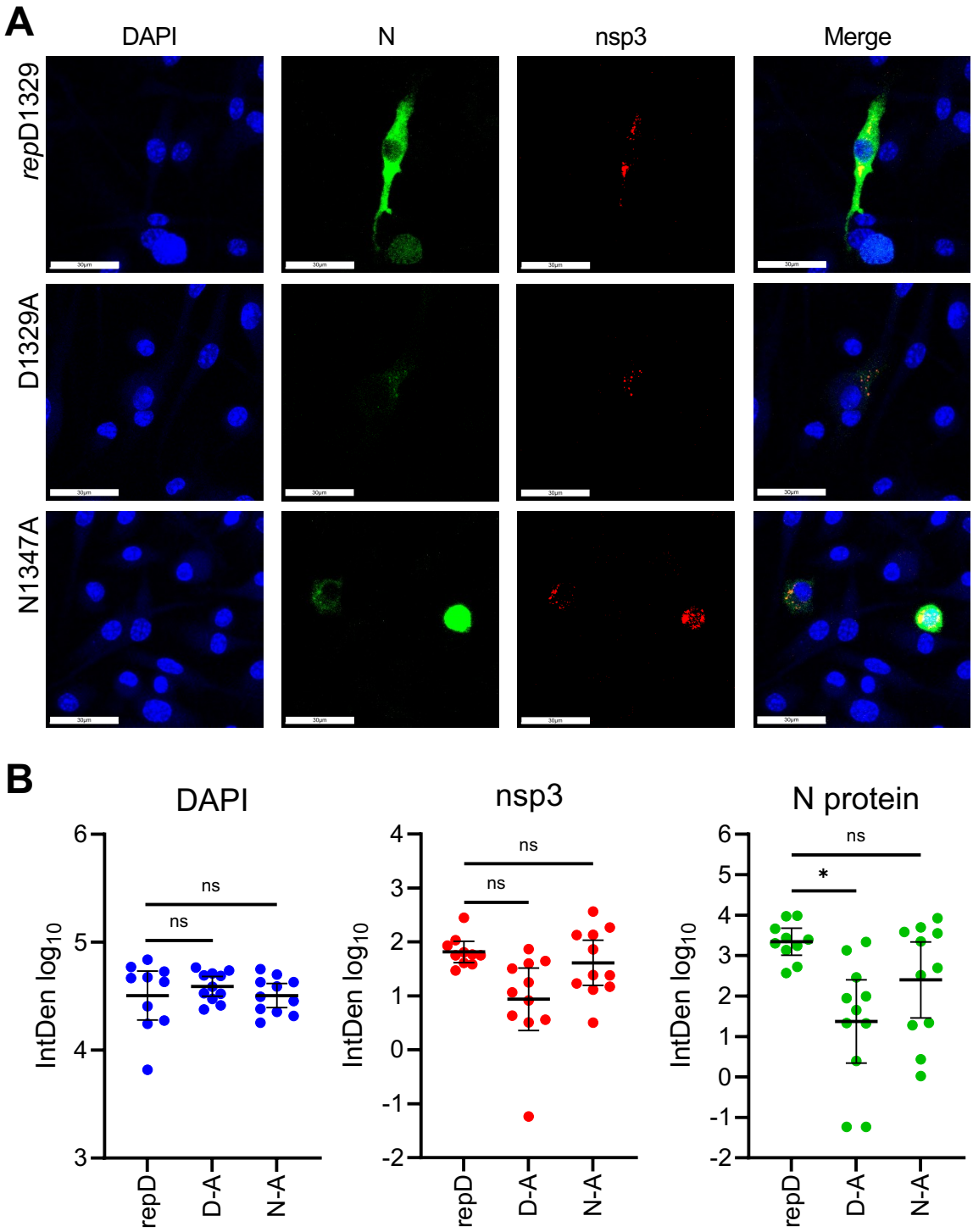

Fig. 8. D1329A and N1347A infected BMDMs have near *rep*D1329 levels of nsp3 but have reduced N protein abundance. (A) BMDMs were infected with indicated virus at an MOI of 0.5 and fixed at 9 hpi, stained for nsp3 and N protein, and analyzed by confocal microscopy. **(B)** Quantification of fluorescence signal displayed as a product of mean pixel intensity and thresholded area (IntDen) for all three fluorescent channels. Combined data from two independent experiments presented as geometric mean with 95% confidence intervals.

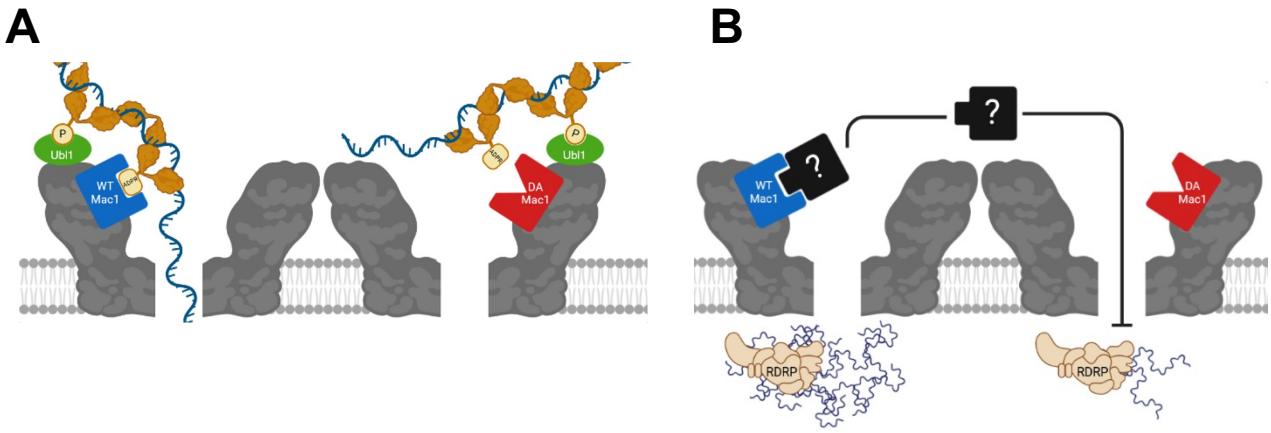

Fig. 9. Potential roles for Mac1 in regulating early RNA transcription. (A) The Ubl1 domain of nsp3 interacts with phosphorylated residues on the RNA-bound nucleocapsid protein which is a key factor in shuttling viral RNA through the nsp3 pore to the site of transcription. Mac1 binding affinity may enhance this interaction between nsp3 and N protein, without which there is a delay in transcription initiation. **(B)** Mac1 binding affinity may sequester or block ADP-ribosylated host factors that target and inhibit viral transcription early in the replication cycle.